# Semiclassical analysis and interpretation of quantum mechanically computed $Cu_2O$ exciton spectra

Master's thesis of
**Moritz Schumacher**

November 24, 2021

Examiner: Prof. Dr. Jörg Main
Co-Examiner: Prof. Dr. Udo Seifert

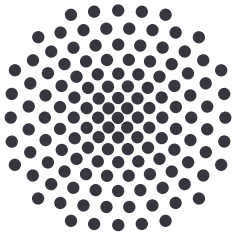

Institut für Theoretische Physik I
Universität Stuttgart
Pfaffenwaldring 57, 70550 Stuttgart

# Contents

# 1 Introduction

In solid state physics the energy dispersion of the electrons is described by the band structure of the solid. When an electron is excited from a valence band into a conduction band it creates an unoccupied state in the valence band which is commonly known as a hole and can be treated as a positively charged quasi particle. Instead of considering all the interactions of the excited electron with the electrons remaining in the valence bands one can equivalently consider only the interaction between the excited electron and the hole. With the Coulomb attraction between those two they can form bound states which are called excitons. This suggests a simple description in analogy to the hydrogen atom which is a good approximation under certain conditions, for example a sufficiently large extension of the exciton such that the crystal background can be treated as a continuum.

In this thesis we consider excitons in cuprous oxide ($Cu_2O$) which can be described as a hydrogen-like system in a first approximation. Depending on the valence bands and conduction bands involved one can distinguish between different exciton series which are named after the corresponding color of light needed for their excitation. The two series with the lowest excitation energies are therefore called yellow and green series. The yellow series with lowest excitation energy has been investigated intensely in experiments and a hydrogen-like exciton spectrum could be observed [1–3]. However also deviations from the hydrogen-like behavior have been found which are visible as a fine-structure splitting in the spectrum [3]. Theoretical investigations could attribute those deviations mainly to the complex band structure of cuprous oxide [4–6]. For a more complete theoretical description of the yellow excitons a present coupling of the yellow and green series has to be taken into account [7]. Therefore the valence bands involved in the green series have to be included. This can be achieved by the introduction of a quasi-spin which couples with the hole spin. The coupling strength of the two series is controlled by the spin-orbit coupling constant $\Delta$. Its value is given by the separation between the valence bands involved in the two series at the $\Gamma$ point.

In 2014 highly excited yellow exciton states with a principal quantum number of up to $n = 25$ could be observe by T. Kazimierczuk et al. in experiments [2]. For those large quantum numbers the correspondence principle becomes applicable and a classical or semiclassical treatment should be possible. In this thesis we want to investigate

connections between the quantum mechanical spectrum and the associated classical dynamics of the yellow excitons. We include the complex valence band structure involved in the yellow and green series and therefore account for the deviations from a hydrogen-like behavior. Numerical calculation of the quantum mechanical exciton spectrum requires the diagonalization of a Hamiltonian using a large but truncated basis set. Although the agreement to experiments is very good [7], those calculations do not provide direct information about the associated classical exciton dynamics. For hydrogen-like systems classical orbits forming Kepler ellipses are connected to the Rydberg spectrum by the Bohr-Sommerfeld model. The classical phase space structure is not changing with energy as all bound states can be connected to classical elliptic Kepler orbits. This is not the case for excitons in $Cu_2O$. The associated classical dynamics is different for every state in the spectrum as the ratio between the corresponding energy and the spin-orbit coupling constant $\Delta$ varies. It is possible to avoid this energy dependence by scaling the coupling constant $\Delta$ with the energy such that the ratio between energy and the resulting scaled coupling constant $\tilde{\Delta}$ remains constant over the whole spectrum. This leads to a scaled quantum spectrum. For every bound classical dynamics characterized by a given energy there exists a corresponding scaled quantum spectrum.

A connection between the scaled quantum mechanical exciton spectra and classical exciton dynamics is established by semiclassical trace formulas [8, 9]. They relate fluctuations of the quantum density of states to a superposition of oscillations with frequencies determined by the period or action of classical periodic orbits. Their amplitudes are related to stability properties of the orbits. We therefore apply a Fourier transform and a technique for high-resolution spectral analysis called harmonic inversion [10, 11] to numerically calculated scaled quantum exciton spectra. The resulting quantum recurrence spectra exhibit peaks at positions given by the action of classical periodic orbits of the associated classical dynamics. Their contribution to the quantum spectra is given by the amplitudes of the peaks.

By appropriately including the band structure of $Cu_2O$ it is possible to treat the excitons classically [12–14]. With the application of semiclassical theories a semiclassical recurrence spectrum can be obtained from parameters of numerically integrated classical periodic orbits [14]. A comparison of the quantum and semiclassical recurrence spectra shows very good agreement. This allows us to obtain information about the periodic orbits (e.g. shape, action, stability, etc.) contributing to the scaled quantum spectra. This thesis thus provides a deeper insight into the classical exciton dynamics in $Cu_2O$ and the relation between the fine-structure splitting present in quantum spectra and the associated classical dynamics.

## 1.1 Structure of the Thesis

This thesis is organized as follows. In chapter 2 we discuss the theoretical foundations and methods for a semiclassical interpretation of quantum spectra of excitons in cuprous oxide. In section 2.1 we first give an overview of the semiconductor cuprous oxide. We discuss its crystal structure, the resulting band structure and the quantum mechanical and classical treatment of excitons in $Cu_2O$. In section 2.2 we give an overview about semiclassical theories and how they can be applied to excitons in cuprous oxide. In section 2.3 we discuss the methods used to obtain the quantum mechanical spectra and the corresponding recurrence spectra.

In chapter 3 we present our results. In section 3.1 we show and discuss the resulting quantum spectra and corresponding recurrence spectra. In section 3.3 we give a brief overview of the results for the classical dynamics. In section 3.3 we then discuss the similar structures between the quantum and the semiclassical recurrence spectra.

# 2 Theory and methodology

## 2.1 Excitons in cuprous oxide

Excitons are created by exciting an electron from the valence band into the conduction band of a semiconductor. The missing electron can be treated as a positively charged particle called hole. Due to the Coulomb attraction between the electron in the conduction band and the hole in the valence band they can form a bound pair called an exciton. Its energy lies below the gap energy. Depending on the strength of the Coulomb attraction there are two limiting cases of strongly and weakly bound excitons. In the first case the exciton is strongly localized at a lattice point and is called a Frenkel exciton [15, 16]. They can be observed for example in ion crystals [17]. In the second case the extension of the exciton is large compared to the lattice constant and is called a Wannier or Mott-Wannier exciton [18]. The latter can be described as hydrogen-like states with a corresponding Rydberg spectrum. This type of excitons can be observed in semiconducturs [17] such as cuprous oxide ($Cu_2O$). Excitons in $Cu_2O$ will be considered in this thesis and we therefore will give a short introduction to this crystal.

Cuprous oxide is a red-colored crystal of high historical importance as the first observations of excitons have been made in it in the 1950s [1]. The comparatively large Rydberg energy of around 100 meV [2] results in a splitting of the energy levels which is in turn comparatively easy to resolve in experiments. Thus even in the earliest experiments excitons with a principal quantum number of up to $n = 9$ could be observed [1]. Advances in experimental methods and tools made it possible to observe excitons up to a principal quantum number of $n = 25$ with a corresponding spacial extension of the wave function of around 2 $\mu$m in 2014 [2]. For the observation of excitons crystals of high purity are needed [19]. As of now those are only available from natural deposits and artificial fabrication is a current field of research [20].

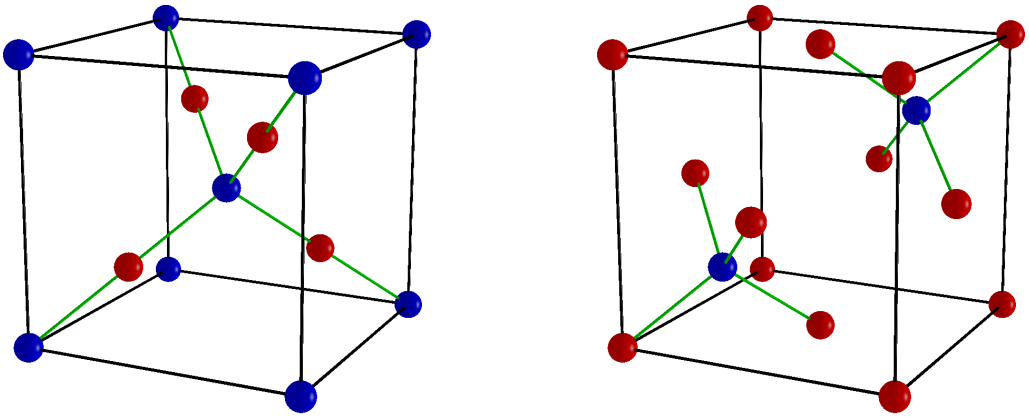

**Figure 2.1:** Two possible choices of the unit cell of cuprous oxide. The oxygen atoms (blue spheres) are arranged in a bcc lattice (left) and the copper atoms (red spheres) in an fcc lattice (right) which are shifted against each other by 1/4 of the space diagonal. The bonds are depicted as green lines.

### 2.1.1 Crystal structure

Cuprous oxide forms a primitive cubic Bravais lattice with lattice constant 0.427 nm [22]. The crystal structure is shown in fig. 2.1 and is created by two cubic lattices, an fcc lattice of copper atoms and a bcc lattice of oxygen atoms, which are shifted against each other by an amount of 1/4 of the space diagonal along the same one [2, 23]. Thus the symmetries are captured by the space group $O_h^4$ in Schoenflies notation or P $4_2$/n $\bar{3}$ 2/m in Hermann–Mauguin notation with corresponding point group $O_\mathrm{h}$. It consists of the following symmetry operations and their equivalents:

- $4_2$/n: rotation by 90° around the [001] axis, shift by 1/2 of the lattice vector and glide translation along half a face diagonal
- $\bar{3}$: rotation by 120° around the [111] axis followed by a space inversion
- 2/m: rotation by 180° around the [011] axis followed by a reflection on the plane perpendicular to the axis

The basis consists of two oxygen and four copper atoms. The symmetry operations of the point group $O_\mathrm{h}$ which is the symmetry group of a cube are given in tab. 2.1.

**Table 2.1:** Symmetry operations of point group $O_\mathrm{h}$. The prepended numbers count the number of equivalent axes or planes [12, 21].

| Symmetry operation | Description |
|---|---|
| E | Identity |
| $8C_3$ | three-fold rotations about the [111] axis and equivalents |
| $3C_2$ | two-fold rotations about the [001] axis and equivalents |
| $6C_4$ | four-fold rotations about the [001] axis and equivalents |
| $6C_2$ | two-fold rotations about the [011] axis and equivalents |
| $I$ | Inversion |
| $8S_6$ | Improper rotations about the [111] axis and equivalents |
| $3\sigma_h$ | Reflection in plane normal to the [001] axis and equivalents |
| $6S_4$ | Improper rotations about the [001] axis and equivalents |
| $6\sigma_d$ | Reflection in plane normal to the [011] axis and equivalents |

### 2.1.2 Band structure

Cuprous oxide is a direct semiconductor with a band structure schematically shown in fig. 2.2. There are two excitations considered in this thesis called yellow and green series after the corresponding colors of the light needed for their excitations [2]. The yellow series corresponds to an excitation from the uppermost valence band to the lowest conduction band. The green series corresponds to an excitation to the lowest conduction band from one of the two valence bands which lie by an amount of $\Delta$ lower than the uppermost valence band. They coincide at $k = 0$, have different curvature and are therefore often referred to as heavy hole and light hole band corresponding to the one with lower and higher curvature, respectively. The one valence band and the two valence bands involved in the yellow and green series, respectively, are each two-fold degenerate [5].

If the exciton wave function of a direct semiconductor extends over a large number of unit cells the effective-mass approximation can be used as a first approximation if we assume non-degenerate isotropic parabolic bands. The corresponding excitons are called Wannier excitons [18]. The large extension of the wave function compared to the lattice constant justifies the use of a static effective dielectric constant $\varepsilon$. The resulting effective Hamiltonian for a series reads [24, 25]

$$H = E_\mathrm{g} + \frac{\boldsymbol{p}_\mathrm{e}^2}{2m_\mathrm{e}} + \frac{\boldsymbol{p}_\mathrm{h}^2}{2m_\mathrm{h}} + V(|\boldsymbol{r}_\mathrm{e} - \boldsymbol{r}_\mathrm{h}|)\,, \tag{2.1}$$

with $\boldsymbol{p}_\mathrm{e}$ and $\boldsymbol{p}_\mathrm{h}$ the momenta operators of the electron and hole, their effective masses $m_\mathrm{e}$ and $m_\mathrm{h}$ and $E_\mathrm{g}$ the energy gap. $V(|\boldsymbol{r}_\mathrm{e} - \boldsymbol{r}_\mathrm{h}|)$ is the Coulomb potential which is screened by the effective relative dielectric constant $\varepsilon$ resulting from the remaining electrons in

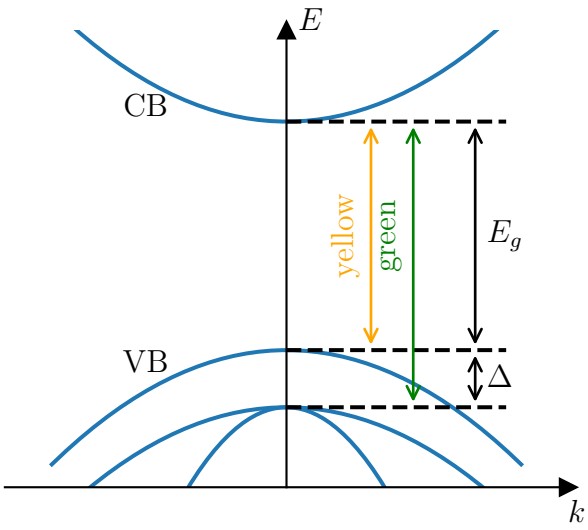


**Figure 2.2:** Schematic representation of the band structure of cuprous oxide around the center of the Brillouin zone. The lowest conduction band (CB) is separated from the highest valence band (VB) by the energy gap $E_g$. The uppermost VB is separated to the two lower lying ones by the spin-orbit coupling constant $\Delta$. The two series shown are named after the corresponding light needed for their excitation.

the valence bands

$$V(|\boldsymbol{r}_e - \boldsymbol{r}_h|) = \frac{e^2}{4\pi\varepsilon_0\varepsilon|\boldsymbol{r}_e - \boldsymbol{r}_h|}\,, \tag{2.2}$$

with $e$ the unit charge and $\varepsilon_0$ the vacuum permittivity. If we introduce relative and center of mass momenta and coordinates

$$\begin{aligned} \boldsymbol{r} &= \boldsymbol{r}_e - \boldsymbol{r}_h\,, & \boldsymbol{R} &= (m_e\boldsymbol{r}_e + m_h\boldsymbol{r}_h)/(m_e + m_h)\,, \\ \boldsymbol{p} &= (m_h\boldsymbol{p}_e - m_e\boldsymbol{p}_h)/(m_e + m_h)\,, & \boldsymbol{P} &= \boldsymbol{p}_e + \boldsymbol{p}_h\,, \end{aligned} \tag{2.3}$$

eq. (2.1) transforms to

$$H = E_g + \frac{\boldsymbol{p}^2}{2\mu} + \frac{\boldsymbol{P}^2}{2M} + \frac{e^2}{4\pi\varepsilon_0\varepsilon|\boldsymbol{r}|}\,, \tag{2.4}$$

with the total mass $M = m_e + m_h$ and reduced mass $\mu = m_e m_h/M$. Neglecting the motion of center of mass $\boldsymbol{P}$ the excitation energy becomes a hydrogen-like Rydberg series

$$E(n) = E_g - \frac{Ry^{\text{exc}}}{n^2}\,, \tag{2.5}$$

with $Ry^{\text{exc}}$ the exciton Rydberg constant

$$Ry^{\text{exc}} = Ry\frac{\mu}{m_0\varepsilon^2} = \frac{\mu e^4}{2(4\pi\varepsilon_0\varepsilon)^2\hbar^2} = \frac{\hbar^2}{2a_{\text{exc}}^2\mu}\,, \tag{2.6}$$

where $m_0$ is the free electron mass and $a_{\text{exc}}$ is the exciton Bohr radius

$$a_{\text{exc}} = a_0\frac{\varepsilon m_0}{\mu} = \frac{4\pi\varepsilon_0\varepsilon\hbar^2}{\mu e^2}\,, \tag{2.7}$$

with $a_0$ the Bohr radius.

The hydrogen-like system of eq. (2.4) exhibits a classical scaling property as the associated classical dynamics does not depend on the energy. Using Bohr's correspondence principle and replacing the coordinate and momentum operators, this can be seen by introducing scaled momenta $\tilde{\boldsymbol{p}} = n\boldsymbol{p}$ and coordinates $\tilde{\boldsymbol{r}} = \boldsymbol{r}/n^2$ with

$$n = \sqrt{-\frac{Ry^{\mathrm{exc}}}{E - E_{\mathrm{g}}}}\,. \tag{2.8}$$

This leads to the classical Hamilton equation

$$\frac{\tilde{\boldsymbol{p}}^2}{2\mu} + \frac{e^2}{4\pi\varepsilon_0\varepsilon|\tilde{\boldsymbol{r}}|} = -Ry^{\mathrm{exc}}\,, \tag{2.9}$$

with center of mass momentum $\boldsymbol{P}$ set to zero. This means that the resulting classical Kepler ellipses only change in size but not their shape when varying the energy. Therefore the classical phase space structure is not changing over the whole Rydberg spectrum which is connected to the classical Kepler ellipses by the Bohr-Sommerfeld model. As we will discuss below, excitons in cuprous oxide deviate from the hydrogen-like case. We will discuss how such a classical scaling property can be recovered in section 2.2.3.

For cuprous oxide eq. (2.4) does not capture the physics well enough as clear systematic deviations from the simple Rydberg series are visible in experiments [3, 26]. Those deviations are the following. Firstly the binding energy of the ground state excitons is much larger than the expected one using the Rydberg energy $Ry^{\mathrm{exc}}$ obtained by the $n > 1$ states [22] which can be explained by their small radii resulting in an intermediate exciton between Frenkel and Wannier. Those deviations can be treated with the so called central-cell corrections affecting all S states [25]. Also a splitting of 1S excitons in para- and ortho-excitons has been observed in experiments [27, 28] and can be described by an exchange interaction of hole and electron spin [25]. We want to neglect those to make use of a scaling property (see section 2.2.3) and to compare the results to semiclassical calculations. Secondly there is a splitting between states of different angular momentum quantum numbers and a threefold splitting of the F excitons visible in the experimentally obtained absorption spectrum of ref. [3]. This indicates that the Runge-Lenz vector and the angular momentum are only approximately conserved quantities and the system has only approximately an SO(4) symmetry.

A more complete model includes the complex valence band structure with cubic symmetry and thereby also accounts for a mixing between yellow and green series present in $Cu_2O$ [6, 25, 29]. For the model used in this thesis the kinetic term for the hole in eq. (2.1) is

replaced by

$$\begin{aligned} H_{\mathrm{h}}(\boldsymbol{p}_{\mathrm{h}}, \boldsymbol{I}, \boldsymbol{S}_{\mathrm{h}}) = & \frac{1}{2\hbar^2 m_0} \left\{ \hbar^2 \left(\gamma_1 + 4\gamma_2\right) \boldsymbol{p}_{\mathrm{h}}^2 + 2\left(\eta_1 + 2\eta_2\right) \boldsymbol{p}_{\mathrm{h}}^2 \left(\boldsymbol{I} \cdot \boldsymbol{S}_{\mathrm{h}}\right) - 6\gamma_2 \left[p_{\mathrm{h}1}^2 I_1^2 + \text{c.p.}\right] \right. \\ & - 12\eta_2 \left[p_{\mathrm{h}1}^2 I_1 S_{\mathrm{h}1} + \text{c.p.}\right] - 12\gamma_3 \left[\{p_{\mathrm{h}1}, p_{\mathrm{h}2}\}\{I_1, I_2\} + \text{c.p.}\right] \\ & \left. -12\eta_3 \left[\{p_{\mathrm{h}1}, p_{\mathrm{h}2}\}\left(I_1 S_{\mathrm{h}2} + I_2 S_{\mathrm{h}1}\right) + \text{c.p.}\right]\right\} + H_{\mathrm{so}}\,, \end{aligned} \tag{2.10}$$

with $\{a, b\} = \frac{1}{2}(ab + ba)$, c.p. denoting cyclic permutation of the components of $\boldsymbol{p}_{\mathrm{h}}$, $\boldsymbol{I}$ and $\boldsymbol{S}_{\mathrm{h}}$. The components of $\boldsymbol{I}$ and $\boldsymbol{S}_{\mathrm{h}}$ are given by the corresponding spin matrices with $I = 1$ and $S_{\mathrm{h}} = \frac{1}{2}$, respectively. Eq. (2.10) includes the valence band structure in the vicinity of the Γ-point by $\boldsymbol{k} \cdot \boldsymbol{p}$-perturbation theory and symmetry considerations [25]. This approximation is justified by the large extension of the exciton wave function in position space and a corresponding small extension in momentum space [30]. The quasi spin $I = 1$ accounts for the three different valence bands involved in the yellow and green series. $\gamma_i$ and $\eta_i$ are the Luttinger parameters [5, 29] and their values (see Appendix A) are obtained by fitting eq. (2.10) to the results of density functional theory calculations [5, 31]. $\gamma_1$ and $\eta_1$ determine the average effective mass of the hole in the different bands and the other ones the splitting and warping, i.e. the dependence of the dispersion on the direction of $\boldsymbol{k}$, of the bands [25, 32]. The last term in eq. (2.10) is the spin-orbit interaction

$$H_{\mathrm{so}} = \frac{2}{3}\Delta \left(1 + \frac{1}{\hbar^2} \boldsymbol{I} \cdot \boldsymbol{S}_{\mathrm{h}}\right)\,, \tag{2.11}$$

with the spin-orbit coupling constant $\Delta$ which is the separation of the yellow and green series at $k = 0$. $H_{\mathrm{so}}$ leads to a coupling between quasi spin $\boldsymbol{I}$ and hole spin $\boldsymbol{S}_{\mathrm{h}}$ to the effective hole spin $J = I + S_{\mathrm{h}}$. The possible values $J = \{1/2, 3/2\}$ distinguish between the yellow $J = 1/2$ and green $J = 3/2$ series. The lowest conduction band involved in the two series considered can be well described by a parabola with isotropic curvature in all directions [5]. Thus the kinetic term for the electron stays in the effective-mass approximation. By expressing $p_{\mathrm{h}/e} = \frac{m_{\mathrm{h}/e}}{M} P \mp p$ and neglecting polariton effects by setting the center of mass momentum $P$ to zero [25], the whole Hamiltonian with the correction eq. (2.10) in center of mass and relative coordinates and momenta reads

$$H = E_{\mathrm{g}} + V(r) + H_{\mathrm{kin}}(\boldsymbol{p}, \boldsymbol{I}, \boldsymbol{S}_{\mathrm{h}}) + H_{\mathrm{so}}(\boldsymbol{I}, \boldsymbol{S}_{\mathrm{h}})\,, \tag{2.12}$$

where $H_{\mathrm{kin}}$ contains all kinetic terms

$$\begin{aligned} H_{\mathrm{kin}}(\boldsymbol{p},\boldsymbol{I},\boldsymbol{S}_{\mathrm{h}}) =& \frac{\gamma_1'}{2m_0}\boldsymbol{p}^2 + \tilde{H}_{\mathrm{kin}}(\boldsymbol{p},\boldsymbol{I},\boldsymbol{S}_{\mathrm{h}}) \\ =& \frac{1}{2\hbar^2 m_0}\left\{\hbar^2(\gamma_1'+4\gamma_2)\boldsymbol{p}^2 + 2(\eta_1+2\eta_2)\boldsymbol{p}^2(\boldsymbol{I}\cdot\boldsymbol{S}_{\mathrm{h}}) - 6\gamma_2\left[p_1^2 I_1^2 + \mathrm{c.p.}\right]\right. \\ & - 12\eta_2\left[p_1^2 I_1 S_{\mathrm{h}1} + \mathrm{c.p.}\right] - 12\gamma_3\left[\{p_1,p_2\}\{I_1,I_2\} + \mathrm{c.p.}\right] \\ & \left. -12\eta_3\left[\{p_1,p_2\}(I_1 S_{\mathrm{h}2} + I_2 S_{\mathrm{h}1}) + \mathrm{c.p.}\right]\right\}, \end{aligned} \tag{2.13}$$

with

$$\gamma_1' = \gamma_1 + \frac{m_0}{m_{\mathrm{e}}}. \tag{2.14}$$

$\tilde{H}_{\mathrm{kin}}(\boldsymbol{p},\boldsymbol{I},\boldsymbol{S}_{\mathrm{h}})$ contains all kinetic terms of the valence band structure differing from the effective-mass approximation. The symmetry of the Hamiltonian (2.12) is reduced by eq. (2.13) to cubic symmetry (point group $O_{\mathrm{h}}$). This can be seen if one writes eq. (2.13) in terms of irreducible tensors [25, 33]. Thus it describes the correct symmetry of the band structure of $Cu_2O$. In the following we set $E_{\mathrm{g}} = 0$ as it only describes an energy shift. The material parameters used in this thesis are given in Appendix A.

To describe the deviations from the Rydberg series caused by the band structure the so called quantum defect $\delta_{n,l}$, which depends on the principal quantum number $n$ and the angular momentum quantum number $l$, is introduced via [4, 34]

$$E_n = -\frac{Ry^{\mathrm{exc}}}{(n-\delta_{n,l})^2} = -\frac{Ry^{\mathrm{exc}}}{n_{\mathrm{eff}}^2}, \tag{2.15}$$

and thereby another quantity $n_{\mathrm{eff}}$ called effective quantum number is introduced which will become the scaling parameter of the scaled system as will be introduced in section 2.2.3. Eq. (2.15) together with eq. (2.7) motivates the introduction of exciton Hartree units (see Appendix B) by setting $\hbar = e = 1$, $\mu = \frac{m_0}{\gamma_1'} = 1$ and $a_{\mathrm{exc}} = a_0\varepsilon\gamma_1' = 1$[1] in analogy to the Hartree atomic units.[2]

### 2.1.3 Classical treatment

Here we give a short overview of how J. Ertl [12, 13] and M. Marquardt [14] treat the Hamiltonian (2.12) classically to calculate corresponding classical exciton orbits. To treat

[1] Setting $a_{\mathrm{exc}} = 1$ is equal to setting $4\pi\varepsilon_0\varepsilon = 1$.

[2] Using $\gamma_1'$ for defining the unit of mass does not couple the unit system to a specific series as both $\gamma_1$ and $\eta_1$ determine the average effective mass of a valence band. For example a unit system coupled to the yellow series would have $\mu = m_0/(\gamma_1' - 2\eta_1) = 1$.

the spin degrees of freedom appropriately it is assumed that the spin dynamics is much faster than the motion of the relative coordinates. Then an adiabatic approach [12, 13] is used with the following separation ansatz for the wave function

$$\Psi = \Phi(\boldsymbol{p})X(\boldsymbol{p};\boldsymbol{I},\boldsymbol{S}_\mathrm{h})\,, \tag{2.16}$$

where $\Phi(\boldsymbol{p})$ only depends on the relative coordinates $\boldsymbol{p}$ and $X(\boldsymbol{p};\boldsymbol{I},\boldsymbol{S}_\mathrm{h})$ depends on the quasi-spin $\boldsymbol{I}$ and hole spin $\boldsymbol{S}_\mathrm{h}$ with $\boldsymbol{p}$ entering as a parameter. Using the ansatz

$$X(\boldsymbol{p};\boldsymbol{I},\boldsymbol{S}_\mathrm{h}) = \sum_{m_I,m_{S_\mathrm{h}}} c_{m_I,m_{S_\mathrm{h}}}(\boldsymbol{p})\,|m_I,m_{S_\mathrm{h}}\rangle\ , \tag{2.17}$$

and collecting all spin-dependent terms of the Hamiltonian (2.12)

$$H_b(\boldsymbol{p},\boldsymbol{I},\boldsymbol{S}_\mathrm{h}) = \tilde{H}_\mathrm{kin}(\boldsymbol{p},\boldsymbol{I},\boldsymbol{S}_\mathrm{h}) + H_\mathrm{so}(\boldsymbol{I},\boldsymbol{S}_\mathrm{h})\,, \tag{2.18}$$

one has to solve the Schrödinger equation

$$H_b(\boldsymbol{p},\boldsymbol{I},\boldsymbol{S}_\mathrm{h})X(\boldsymbol{p};\boldsymbol{I},\boldsymbol{S}_\mathrm{h}) = W_n(\boldsymbol{p})X(\boldsymbol{p};\boldsymbol{I},\boldsymbol{S}_\mathrm{h})\,, \tag{2.19}$$

which is done numerically by solving the corresponding six-dimensional eigenvalue problem. The spectrum with cardinality six consists of three two-fold degenerate eigenvalues $W_n(\boldsymbol{p})$ due to the degeneracy of the bands. They represent energy surfaces in momentum space. Using the ansatz (2.16) the Schrödinger equation with the full Hamiltonian reads in exciton Hartree units

$$H\Phi X = X\left[\frac{1}{2}\boldsymbol{p}^2 - \frac{1}{r}\right]\Phi + \Phi H_b X - \frac{1}{r}\left(\Phi X\right) + X\frac{1}{r}\Phi\,, \tag{2.20}$$

where the last two terms, occurring because of the $\boldsymbol{p}$-dependence of $X$, would couple the different energy surfaces $W_n$ and is neglected in the adiabatic approximation by assuming that the spin dynamics reacts instantaneously to changes due to the movement of the relative coordinates. Thus the Hamiltonian for the relative coordinates reads

$$\tilde{H} = \frac{1}{2}\boldsymbol{p}^2 - \frac{1}{r} + W_n(\boldsymbol{p})\,, \tag{2.21}$$

where the lowest energy surface $W_n(\boldsymbol{p})$ can be assigned to the yellow series. Using Bohr's correspondence principle one can replace the coordinate and momentum operators with the corresponding classical variables. Classical orbits are then calculated by integrating the corresponding Hamilton's equation of motion numerically. By variation of the initial coordinates and momenta periodic orbits are then searched. The additional integration of the action allows for determining the action-angle coordinates. Further details can be found in refs. [12] and [14].

## 2.2 Semiclassical theories and their application to excitons in cuprous oxide

Semiclassical trace formulas connect the quantum mechanical density of states with classical orbits of the corresponding classical system. In section 2.2.1 we first outline the derivation of the EBK quantization condition and then introduce and discuss the Berry-Tabor formula for integrable systems and Gutzwiller's trace formula for chaotic systems. We then discuss the application of those formulas for excitons in cuprous oxide. In section 2.2.2 we discuss why it is advantageous for a system to posses a scaling property if we want to interpret the quantum mechanical spectrum semiclassically. The Hamiltonian (2.12) for excitons in cuprous oxide introduced in section 2.1.2 lacks a scaling property. We describe how it can be modified to posses a scaling property in section 2.2.3.

### 2.2.1 Semiclassical trace formulas and their application for excitons in cuprous oxide

In the following we follow J. E. Bayfield [35] and S. Wimberger [36]. We assume an integrable system (number of degrees of freedom equals the number of constants of motion) and start with the stationary Schrödinger equation

$$\left(-\frac{\hbar^2}{2m}\nabla^2 + V(\boldsymbol{r})\right)\psi(\boldsymbol{r}) = E\psi(\boldsymbol{r})\,. \tag{2.22}$$

Inserting the ansatz

$$\phi(\boldsymbol{r}) = A(\boldsymbol{r})e^{\frac{i}{\hbar}S(\boldsymbol{r})}\,, \tag{2.23}$$

with real-valued functions $A$ and $S$ into (2.22) the real-valued part reads

$$\left[\frac{\nabla S(\boldsymbol{r})}{2m} + V(\boldsymbol{r})\right] = E + \frac{\hbar^2}{2m}\frac{\nabla^2 A(\boldsymbol{r})}{A(\boldsymbol{r})}\,, \tag{2.24}$$

and the imaginary part

$$\nabla\left(A^2(\boldsymbol{r})\nabla S(\boldsymbol{r})\right) = 0\,. \tag{2.25}$$

Neglecting the terms of order $\mathcal{O}(\hbar^2)$ the real part (2.24) is the Hamilton-Jacobi equation with $S$ being Hamilton's characteristic function. Since we assumed an integrable system we can transform to action-angle variables $(\boldsymbol{I}, \boldsymbol{\theta})$ such that

$$S(\boldsymbol{r}, \boldsymbol{I}) = \int_{\boldsymbol{r}_0}^{\boldsymbol{r}} \boldsymbol{p}(\boldsymbol{r}', \boldsymbol{I})\,\mathrm{d}\boldsymbol{r}'\,, \tag{2.26}$$

which is the classical action and as an $F_2$-type generating function of the transformation it follows that

$$\boldsymbol{\theta} = \nabla_{\boldsymbol{I}} S(\boldsymbol{r}, \boldsymbol{I}) \,, \qquad \boldsymbol{p} = \nabla_{\boldsymbol{r}} S(\boldsymbol{r}, \boldsymbol{I}) \,. \tag{2.27}$$

From the imaginary part (2.25) one can derive for the amplitude

$$A^2 \propto \left| \det \left( \frac{\partial \boldsymbol{\theta}}{\partial \boldsymbol{r}} \right) \right| = \left| \det \left( \frac{\partial^2 S}{\partial \boldsymbol{r} \partial \boldsymbol{I}} \right) \right| \,. \tag{2.28}$$

Thus the wave function of the ansatz (2.23) reads

$$\phi(\boldsymbol{r}) = \text{const.} \left| \det \left( \frac{\partial^2 S}{\partial \boldsymbol{r} \partial \boldsymbol{I}} \right) \right|^{\frac{1}{2}} e^{i \frac{S(\boldsymbol{r}, \boldsymbol{I})}{\hbar} + i \frac{\pi}{2} \mu} \,, \tag{2.29}$$

with a constant phase factor $\frac{\pi}{2}\mu$ which will be discussed shortly. Defining the actions $I_i$ on an $N$-dimensional torus in phase space by

$$I_i = \frac{1}{2\pi} \oint_{C_i} \boldsymbol{p} \mathrm{d}\boldsymbol{r} \,, \tag{2.30}$$

where $C_i$ are the elementary loops which build up the basis of a $N$-torus, leading to the formation of overlapping pieces, called layers or leaves when projecting into coordinate space. Thus $\phi(\boldsymbol{r})$ is a multivalued function of $\boldsymbol{r}$ with different branches $j$. The general wave function is therefore the sum over all possible branches

$$\phi(\boldsymbol{r}) = \text{const.} \sum_j \left| \det \left( \frac{\partial^2 S_j}{\partial \boldsymbol{r} \partial \boldsymbol{I}} \right) \right|^{\frac{1}{2}} e^{i \frac{S_j(\boldsymbol{r}, \boldsymbol{I})}{\hbar} + i \frac{\pi}{2} \mu_j} \,. \tag{2.31}$$

As

$$A^2 \propto \left| \det \left( \frac{\partial^2 S}{\partial \boldsymbol{r} \partial \boldsymbol{I}} \right) \right| = \left| \det \left( \frac{\partial \boldsymbol{\theta}}{\partial \boldsymbol{p}} \right) \det \left( \frac{\partial \boldsymbol{p}}{\partial \boldsymbol{r}} \right) \right| \,, \tag{2.32}$$

singularities of $\phi(\boldsymbol{r})$ occur at caustics, which are the generalizations of turning points in one-dimensional systems and thus also called turning surfaces, where the last determinant in eq. (2.32) becomes infinite. To overcome those singularities one can switch to momentum space if a caustic is approached and back to position space if a caustic in momentum space is approached. The wave functions are then "stitched" together to form the global semiclassical wave function. The total accumulated phase along the loop $C_i$ is then

$$\frac{\Delta \phi_i}{\hbar} = \frac{1}{\hbar} \oint_{C_i} \boldsymbol{p} \mathrm{d}\boldsymbol{r} - \frac{\pi}{2} \mu_i = \frac{2\pi}{\hbar} I_i - \frac{\pi}{2} \mu_i \,, \tag{2.33}$$

which has to be a multiple of $2\pi$ for the wave functions to be unique. This leads to the EBK quantization condition

$$\boldsymbol{I} = \hbar \left( \boldsymbol{n} + \frac{\boldsymbol{\mu}}{4} \right) \,, \tag{2.34}$$

with the vector of integer quantum numbers $\boldsymbol{n}$ and $\boldsymbol{\mu}$ the vector of the so called Maslov indices, which counts the number of reflections or more generally focus points or caustics within each loop $C_i$ in phase space, i.e. where bundles of trajectories meet in coordinate space by projection of $C_i$ onto the latter. It therefore accounts for the accumulated phase changes because of all caustics passed during a loop. For example it follows that for rotations $\mu_i = 0$ and vibrations/librations $\mu_i = 2$. With $E = H(\boldsymbol{I})$ it follows for the EKB semiclassical energy levels that

$$E_{\boldsymbol{n}} = H\left(\hbar\left(\boldsymbol{n} + \frac{\boldsymbol{\mu}}{4}\right)\right) . \tag{2.35}$$

As the energy is constant on a torus it follows that only specific tori are semiclassically allowed. One has to note that the paths $C_i$ are not the periodic orbits. As the frequency on the path $C_i$ is

$$\omega_i = \frac{\partial H}{\partial I_i} , \tag{2.36}$$

only if all frequency ratios are given by rational numbers the orbits are periodic and one speaks of resonant tori. In this case winding numbers $M_i$ can be used to characterize the orbits. Those are the number of cycles around the paths $C_i$ needed for a full period of the orbit. Using the quantization condition (2.34) Berry and Tabor connected the density of states to classical periodic orbits [8, 37]. For $N = 2$ dimensions it reads [38]

$$\rho(E) = \tilde{\rho}(E) + \sum_{\boldsymbol{M}\neq 0} \frac{\mathrm{d}S_{\boldsymbol{M}}/\mathrm{d}E}{\pi\sqrt{\hbar^3 M_2^3 |g_E''|}} \cos\left(\frac{S_{\boldsymbol{M}}}{\hbar} - \frac{\pi}{2}\sigma_{\boldsymbol{M}} - \frac{\pi}{4}\right) , \tag{2.37}$$

where $\tilde{\rho}(E)$ denotes the average density of states and is called the Thomas-Fermi or Weyl term. To the second oscillating term only periodic orbits with winding numbers $\boldsymbol{M} = (M_1, M_2)$ contribute, where $M_i$ are positive integer numbers [37]. Furthermore $S_{\boldsymbol{M}}$ denotes the action and $\sigma_{\boldsymbol{M}}$ the Maslov index of the periodic orbit. $\mathrm{d}S_{\boldsymbol{M}}/\mathrm{d}E$ gives the period of the orbit $T_{\boldsymbol{M}}$ but we have written it in a more general form which is needed later. The function $g_E(I_1) = I_2$ is defined by $H(I_1, I_2 = g_E(I_1)) = E = \text{const.}$ and thus describes the curves of constant energy in action space. It can be calculated numerically with the use of the relation

$$S_{\boldsymbol{M}} = 2\pi M_1 J_1 + 2\pi M_2 J_2 . \tag{2.38}$$

By fixing $M_2$ and varying $M_1$ one can determine $J_1$ by numerical differentiation with respect to $M_1$. Having the value of $J_1$ eq. (2.38) can be used to determine $J_2$.

The sum in eq. (2.37) can be decomposed into a sum over all primitive periodic orbits with winding numbers $\tilde{\boldsymbol{M}}$ and their repetitions $l \in \mathbb{N}$

$$\rho_{\mathbb{fl}}(E) = \sum_{\tilde{\boldsymbol{M}}\neq 0} \sum_{l=1}^{\infty} \frac{l\,\mathrm{d}S_{\tilde{\boldsymbol{M}}}/\mathrm{d}E}{\pi\sqrt{\hbar^3 (l\tilde{M}_2)^3 |g_E''|}} \cos\left(\frac{l S_{\tilde{\boldsymbol{M}}}}{\hbar} - \frac{\pi}{2} l\sigma_{\tilde{\boldsymbol{M}}} - \frac{\pi}{4}\right) . \tag{2.39}$$

When adding a non-integrable perturbation to the integrable system the Poincaré-Birkhoff theorem states that the resonant tori break up leaving pairs of isolated stable and unstable periodic orbits behind. For isolated and unstable periodic orbits Gutzwiller derived a semiclassical formula for the density of states. As the starting point he used the relation of the latter to the trace of the quantum mechanical Green's operator and replaced it with a semiclassical approximation. For this he applied a stationary phase approximation to the Feynman path integral leading to the Van-Vleck propagator. Applying another stationary phase approximation to the time integral leads to the semiclassical Greens function which only accounts for classical trajectories at fixed energy. Using another stationary phase approximation and a transformation into coordinates parallel and perpendicular to classical orbits he finally arrived at his trace formula [9, 36]

$$\rho(E) = \tilde{\rho}(E) + \rho_{\text{fl}}(E) = \tilde{\rho}(E) + \frac{1}{\pi\hbar} \sum_{\text{PO}} \frac{\mathrm{d}S_{\text{PPO}}/\mathrm{d}E}{\sqrt{|\det(M_{\text{PO}} - 1)|}} \cos\left(\frac{S_{\text{PO}}}{\hbar} - \frac{\pi}{2}\sigma_{\text{PO}}\right), \quad (2.40)$$

where the subscript PPO denotes the primitive periodic orbit, i.e. one cycle of the orbit, and the subscript PO the periodic orbit, i.e. with possible repetitions of the primitive periodic orbit. $S_{\text{PO}}$ denotes the action and $\sigma_{\text{PO}}$ the Maslov index of the periodic orbit. The symplectic monodromy matrix or stability matrix $M_{\text{PO}}$ describes the linear response of a periodic orbit to a small perturbation perpendicular to the orbit. It is therefore a $(2N-2) \times (2N-2)$ matrix if $N$ denotes the degrees of freedom. As in the Berry-Tabor formula eq. (2.37) $\tilde{\rho}(E)$ denotes the Thomas-Fermi term. The sum in the fluctuating part of eq. (2.40) runs over all periodic orbits and can thus be decomposed formally into all primitive periodic orbits and their repetitions $l \in \mathbb{N}$

$$\rho_{\text{fl}}(E) = \frac{1}{\pi\hbar} \sum_{\text{PPO}} \sum_{l=1}^{\infty} \frac{\mathrm{d}S_{\text{PPO}}/\mathrm{d}E}{\sqrt{|\det\left(M_{\text{PPO}}^{l} - 1\right)|}} \cos\left(l\frac{S_{\text{PPO}}}{\hbar} - l\frac{\pi}{2}\sigma_{\text{PPO}}\right). \quad (2.41)$$

The dynamics for excitons in cuprous oxide turns out to be regular in most parts of the phase space exhibiting one- to three-dimensional tori and thus can be characterized by integer winding numbers $M_i$ [13, 14]. For these orbits only one pair of eigenvalues of the stability matrix $M_{\text{PO}}$ in Gutzwiller's trace formula differs from a value of one, and thus only one unstable direction exists. This would result in singularities in Gutzwiller's trace formula. Therefore for the calculation of the amplitude a mixed approach is used, where the regular two-dimensional subsystem in Gutzwiller's trace formula is replaced by a Berry-Tabor contribution, resulting in the mixed amplitude [14]

$$A_{\text{PO}} = \frac{1}{\pi} \frac{1}{\sqrt{|\lambda_\perp + 1/\lambda_\perp - 2|}} \frac{\mathrm{d}S_{\text{PO}}/\mathrm{d}E}{\sqrt{\hbar^3 M_2^3 |g_E''|}}, \quad (2.42)$$

where here the winding numbers $\boldsymbol{M} = (M_1, M_2)$ count the number of Kepler ellipses and the cycles of secular motion. Secular motion refers to the motion of the Kepler

ellipses along angular coordinates in a spherical coordinate system, i.e. a rotation along the azimuthal angle and an oscillation along the polar angle. For planar orbits, e.g. the orbits in the nine symmetry planes of the $O_\mathrm{h}$-group (see tab. 2.1), there is only a rotation around the origin present. Fully three-dimensional orbits can be seen as having an additional oscillation out of the plane. The secular motion can further be decomposed into the motion along azimuthal and polar angle thereby replacing one winding number with two counting the cycles along each angle. Thus a three-dimensional orbit can be characterized in more detail with the use of three winding numbers. There are also isolated nearly-circular orbits present for which Gutzwiller's trace formula can be used without modification.

### 2.2.2 Application of a scaling property to the recurrence spectrum

Both Berry-Tabor and Gutzwiller's trace formula can be written in the form

$$\rho(E) = \tilde{\rho}(E) + \mathrm{Re} \sum_{\mathrm{PPO}} \sum_{l=1}^{\infty} A_{\mathrm{PPO},l}(E) e^{\frac{ilS_{\mathrm{PPO}}(E)}{\hbar}} , \tag{2.43}$$

thereby absorbing constants and constant phase factors into the amplitude $A_{\mathrm{PPO},l}(E)$. Approximating the action $S_{\mathrm{PPO}}(E)$ up to first order gives in the neighborhood of $E = E_0$

$$S(E) = S(E_0) + \left.\frac{dS}{dE}\right|_{E_0} \Delta E + \mathcal{O}(\Delta E^2) = S(E_0) + T_0 \Delta E + \mathcal{O}(\Delta E^2) , \tag{2.44}$$

with the energy $E_0$, the time period $T_0$ of the orbit, and $\Delta E = E - E_0$. Thus the density of states (2.43) is locally given as a superposition of sinusoidal oscillations. This suggests that a Fourier transform from the energy to the time domain could be used to identify the amplitudes $A_{\mathrm{PPO,r}}$ and time periods $T_{\mathrm{PO}}$ in the quantum spectrum. As $\delta$-peaks at the recurrence time $t = T_0$ would appear the Fourier transformed spectrum is often called recurrence spectrum. In general the actions and amplitudes are non-trivial functions of the energy. Because of the former the linearization of eq. (2.44) is in general only valid locally and the periods $T_0$ change within the spectrum. Thus in general the Fourier transform can only be used for identifying local periodic orbit contributions to the quantum spectrum. For systems with a classical scaling property one can overcome this problem with the use of scaling techniques [10]. In such systems the classical dynamics do not depend on an external scaling parameter $w$. An example are hydrogen-like systems where the classical dynamics and thus the phase space structure stays the same for every state in the connected Rydberg spectrum (see discussion in section 2.1.2). Using appropriately scaled coordinates $\tilde{\boldsymbol{r}}$ and momenta $\tilde{\boldsymbol{p}}$ the action can be expressed as

$$S_{\mathrm{PPO}} = \oint_{\mathrm{PPO}} \boldsymbol{p} \, \mathrm{d}\boldsymbol{r} = w \oint_{\mathrm{PPO}} \tilde{\boldsymbol{p}} \, \mathrm{d}\tilde{\boldsymbol{r}} = w \tilde{S}_{\mathrm{PPO}} , \tag{2.45}$$

with the scaled action $\tilde{S}_{\mathrm{PPO}}$ which is independent of $w$ and thus the action scales linearly with the scaling parameter. For a quantum system application of the scaling technique results in a quantization of the scaling parameter $w$. The spectrum of the latter in the semiclassical approximation is given by

$$\rho(w) = \tilde{\rho}(w) + \mathrm{Re} \sum_{\mathrm{PPO}} \sum_{l=1}^{\infty} A_{\mathrm{PPO},l} e^{\frac{i l \tilde{S}_{\mathrm{PPO}} w}{\hbar}} , \tag{2.46}$$

with an amplitude $A_{\mathrm{PPO},l}$ which is independent of $w$, i.e.

$$A_{\mathrm{PPO},l} \propto \frac{\mathrm{d}S_{\mathrm{PPO}}(w)}{\mathrm{d}w} = \tilde{S}_{\mathrm{PPO}} \, . \tag{2.47}$$

As can be seen in eq. (2.46) the scaling parameter can be interpreted as an effective Planck constant $\hbar_{\mathrm{eff}} = \hbar/w$. This means that the semiclassical limit is approached for increasing values of the quantized scaling parameter of the scaled quantum system. The classical dynamics does not depend on $\hbar_{\mathrm{eff}}$ and thus stays the same for all states in the spectrum. Fourier transform of the fluctuating part of eq. (2.45), with $\hbar = 1$, results in

$$\begin{aligned} \hat{\rho}(\tilde{S}) =& \frac{1}{2\pi} \sum_{\mathrm{PPO}} \sum_{l=1}^{\infty} \int_{-\infty}^{+\infty} \frac{1}{2} \left( A_{\mathrm{PPO},l} e^{i l \tilde{S}_{\mathrm{PPO}} w} + A^*_{\mathrm{PPO},l} e^{-i l \tilde{S}_{\mathrm{PPO}} w} \right) e^{-i \tilde{S} w} \, \mathrm{d}w \\ =& \frac{1}{2} \sum_{\mathrm{PPO}} \sum_{l=1}^{\infty} \left( A_{\mathrm{PPO},l} \delta(\tilde{S} - l\tilde{S}_{\mathrm{PPO}}) + A^*_{\mathrm{PPO},l} \delta(\tilde{S} + l\tilde{S}_{\mathrm{PPO}}) \right) . \end{aligned} \tag{2.48}$$

This enables one to directly identify periodic orbits by their scaled action $\tilde{S}_{\mathrm{PO}} = l\tilde{S}_{\mathrm{PPO}}$ as $\delta$-peaks appearing in the recurrence spectrum $\hat{\rho}(\tilde{S})$ at positions $\tilde{S} = \pm\tilde{S}_{\mathrm{PO}}$. Their strengths are given by the amplitudes $A_{\mathrm{PPO},l}$.

### 2.2.3 Applying scaling techniques to excitons in cuprous oxide

As described in the previous section 2.2.2 we need a scaling property of the Hamiltonian to be able to directly identify contributions of classical periodic orbits to the quantum mechanical density of states. The Hamiltonian (2.12) possesses a scaling property if the spin-orbit term $H_{\mathrm{SO}}$ is excluded. To see this we first notice that in the kinetic part (2.13) of the Hamiltonian (2.12) the momentum operator only occurs in quadratic order. Secondly, we can express the energy with the use of eq. (2.15). In exciton Hartree units the Schrödinger equation of our system without the spin-orbit term reads

$$H \left| \Psi \right\rangle = \left[ \frac{1}{2} \boldsymbol{p}^2 + \boldsymbol{p} L \boldsymbol{p} - \frac{1}{r} \right] \left| \Psi \right\rangle = -\frac{1}{2 n_{\mathrm{eff}}^2} \left| \Psi \right\rangle , \tag{2.49}$$

where we expressed $\tilde{H}_{\mathrm{kin}}(\boldsymbol{p}, \boldsymbol{I}, \boldsymbol{S}_{\mathrm{h}})$ introduced in eq. (2.13) with the use of a Hermitian linear operator $L$ which depends on the quasi spin and hole spin. We can multiply eq. (2.49) formally with $n_{\mathrm{eff}}^2$ which yields

$$\left[\frac{1}{2}(n_{\mathrm{eff}}\boldsymbol{p})^2 + n_{\mathrm{eff}}\boldsymbol{p}Ln_{\mathrm{eff}}\boldsymbol{p} - \frac{n_{\mathrm{eff}}^2}{r}\right]|\Psi\rangle = -\frac{1}{2}|\Psi\rangle\ . \tag{2.50}$$

With the adiabatic approach we can replace $n_{\mathrm{eff}}\boldsymbol{p}Ln_{\mathrm{eff}}\boldsymbol{p}$ by an energy surface $\bar{W}(n_{\mathrm{eff}}\boldsymbol{p})$. Thus the classical Hamiltonian reads

$$\frac{1}{2}(n_{\mathrm{eff}}\boldsymbol{p})^2 + \bar{W}(n_{\mathrm{eff}}\boldsymbol{p}) - \frac{n_{\mathrm{eff}}^2}{r} = -\frac{1}{2}\,. \tag{2.51}$$

By introducing scaled momenta $\tilde{\boldsymbol{p}} = n_{\mathrm{eff}}\boldsymbol{p}$ and coordinates $\tilde{\boldsymbol{r}} = \boldsymbol{r}/n_{\mathrm{eff}}^2$ the Hamiltonian becomes independent of $n_{\mathrm{eff}}$ and also the classical dynamics

$$\frac{1}{2}\tilde{\boldsymbol{p}}^2 + \bar{W}(\tilde{\boldsymbol{p}}) - \frac{1}{\tilde{r}} = -\frac{1}{2}\,. \tag{2.52}$$

$n_{\mathrm{eff}}$ plays the role of a scaling parameter. Adding the spin-orbit term destroys the scaling property as we thereby introduce a term independent of the momentum and coordinate operators. Therefore the introduction of scaled variables does not result in the corresponding classical Hamiltonian to be independent of the scaling parameter $n_{\mathrm{eff}}$. We can recover the scaling property by replacing the coupling constant $\Delta$ in eq. (2.11) with an energy-dependent coupling parameter

$$\Delta \to \tilde{\Delta} = \frac{n_0^2}{n_{\mathrm{eff}}^2}\Delta\,, \tag{2.53}$$

with a constant parameter $n_0$ controlling the strength of the scaled spin-orbit coupling. With the use of eq. (2.53) the Schrödinger equation multiplied by $n_{\mathrm{eff}}^2$ reads

$$\left[\frac{1}{2}(n_{\mathrm{eff}}\boldsymbol{p})^2 - \frac{n_{\mathrm{eff}}^2}{r} + n_{\mathrm{eff}}\boldsymbol{p}Ln_{\mathrm{eff}}\boldsymbol{p} + \frac{2}{3}n_0^2\Delta\,(1 + \boldsymbol{I}\cdot\boldsymbol{S}_{\mathrm{h}})\right]|\Psi\rangle = -\frac{1}{2}|\Psi\rangle\ . \tag{2.54}$$

Applying the adiabatic approach now including the new spin-orbit term and using the same scaled variables the classical Hamiltonian is

$$\frac{1}{2}\tilde{\boldsymbol{p}}^2 + W_{n_0}(\tilde{\boldsymbol{p}}) - \frac{1}{\tilde{r}} = -\frac{1}{2}\,, \tag{2.55}$$

where now the energy surface $W_{n_0}(\tilde{\boldsymbol{p}})$ depends on the parameter $n_0$ and thus also the classical dynamics. To circumvent the calculation of $W_{n_0}(\tilde{\boldsymbol{p}})$ for each choice of $n_0$ we take advantage of the fact that an arbitrary reference system can be chosen to calculate the classical orbits. We only have to scale the resulting quantities accordingly afterwards.

Using $n_{\text{eff}} = n_0$ recovers the original coupling constant $\tilde{\Delta} = \Delta$ and thus is an appropriate choice. We can now calculate the orbits in the usual variables $\boldsymbol{p}$ and $\boldsymbol{r}$ using the Hamiltonian (2.21). The scaled versions of them then satisfy eq. (2.55). This means that the value of $n_0$ specifies the classical exciton dynamics to the one of the unscaled system at fixed energy $E = -1/2n_0^2$.

When introducing scaled variables for the quantum mechanical case they have to satisfy the canonical commutation relations. Therefore as we choose for the coordinate operator $\tilde{\boldsymbol{r}} = \boldsymbol{r}/n_{\text{eff}}^2$ the scaled momentum operator has to be $\tilde{\boldsymbol{p}} = n_{\text{eff}}^2\boldsymbol{p}$. With the use of those variables we can transform eq. (2.54) into the generalized eigenvalue problem

$$\tilde{H}\,|\Psi\rangle = \lambda_k H_{\text{kin}}(\tilde{\boldsymbol{p}}, \boldsymbol{I}, \boldsymbol{S}_{\text{h}})\,|\Psi\rangle\ , \tag{2.56}$$

with

$$\tilde{H} = \frac{1}{\tilde{r}} - n_0^2 H_{\text{SO}}(\boldsymbol{I}, \boldsymbol{S}_{\text{h}}) - \frac{1}{2}\,, \tag{2.57}$$

where the eigenvalues are $\lambda_k = 1/n_{\text{eff},k}^2$ and thus the scaling parameter $w = n_{\text{eff}}$ is quantized as mentioned in the previous section 2.2.2. As $n_0$ is a constant parameter the classical dynamics is the same for all states in the spectrum of the scaled quantum system. This allows for a comparison between the classical dynamics at given energy and the corresponding quantum mechanics. With the use of eq. (2.48) Fourier transform in the variable $n_{\text{eff}}$ of the quantum mechanical density of states

$$\rho(n_{\text{eff}}) = \sum_k \delta(n_{\text{eff}} - n_{\text{eff},k})\,, \tag{2.58}$$

into the scaled action domain $\tilde{S}$ should result in $\delta$-peaks at the scaled actions $\tilde{S}_{\text{PO}}$ of the periodic orbits of the underlying classical exciton dynamics. Their amplitudes should correspond to the semiclassical amplitudes $A_{\text{PPO},l}$. For the isolated central orbit the amplitude reads (in exciton Hartree units)

$$A_{\text{PPO},l}^{\text{central}} = \frac{1}{\pi}\frac{\tilde{S}_{\text{PPO}}}{\sqrt{|\det\left(M_{\text{PPO}}^l - 1\right)|}} e^{-il\frac{\pi}{2}\sigma_{\text{PPO}}}\,, \tag{2.59}$$

and for the mixed amplitude (2.42)

$$A_{\text{PPO},l}^{\text{mixed}} = \frac{1}{\pi}\frac{1}{\sqrt{|\lambda_\perp^l + 1/\lambda_\perp^l - 2|}}\frac{l\tilde{S}_{\text{PPO}}}{\sqrt{(lM_2)^3|g_{n_0}''|}} e^{-i\left(l\frac{\pi}{2}\sigma_{\boldsymbol{M}} + \frac{\pi}{4}\right)}\,, \tag{2.60}$$

where $g_{n_0}$ now depends on the parameter $n_0$ instead of the energy $E$.

## 2.3 Methods

In the following we first discuss in section 2.3.1 the basis set used for numerical calculation of the quantum spectra and the structure of the resulting matrix equation. We further discuss the behavior of the eigenvalues when using a finite basis set. We then give in section 2.3.2 a short discussion about what needs to be considered when using the conventional Fourier transform of the quantum mechanical density of states for obtaining the corresponding recurrence spectrum and its limitations. We then discuss in section 2.3.3 the technique of harmonic inversion which can be used to circumvent those limitations.

### 2.3.1 Numerical calculation of the quantum spectra

The basis set used in this thesis to solve the Schrödinger equation with the Hamiltonian (2.12) and the generalized eigenvalue problem (2.56) is the following

$$|\Pi\rangle = |N, L, J, F, M_F\rangle \ , \tag{2.61}$$

with $N$ the radial quantum number which is connected to the principal quantum number $n$ via $N = n - L - 1$ and $L$ the angular momentum quantum number. As already stated in section 2.1.2 $I$ and $S_h$ are coupled via the spin-orbit coupling term $H_{\text{so}}$ to the effective hole spin $J$. In the spherical approximation of eq. (2.13), which neglects all cubic terms, the total angular momentum $F = J + L$ and its $z$-component $M_F$ are good quantum numbers [25, 39] and are thus used in the basis to be close to an eigenbasis. As the central-cell corrections and the exchange interaction are not included in our model, the electron spin $S_e$ and its $z$-component $M_{S_e}$ are good quantum numbers. They only result in a degeneracy of the eigenstates and thus are not included in our basis. The possible values of the quantum numbers for a given $n$ are

$$\begin{aligned} L &= 0, \ldots, n-1 \,, \\ J &= 1/2, 3/2 \,, \\ F &= |L - J|, \ldots, L + J \,, \\ M_F &= -F, \ldots, +F \,. \end{aligned} \tag{2.62}$$

As the Hamiltonian (2.12) is hydrogen-like without the valence band structure terms, an expansion basis in terms of the hydrogen-like eigenfunctions seems appropriate. But without the difficult inclusion of the continuum functions they do not form a complete set of basis functions. Therefore the closely related Coulomb-Sturmian functions are used. The basis functions are called Coulomb-Sturmian functions as they are the solutions to a

Sturm-Liouville eigenproblem with the Coulomb potential as the weighting function [40]. The radial part reads [25]

$$U_{NL}(r) = N_{NL}\ (2\rho)^L e^{-\rho} L_N^{2L+1}(2\rho)\,, \tag{2.63}$$

with the associated Laguerre polynomials $L_N^{2L+1}(x)$, $\rho = r/\alpha$ and $\alpha$ an arbitrary positive real scaling parameter. The normalization factor $N_{NL}$ reads

$$N_{NL} = \frac{2}{\sqrt{\alpha^3}} \left[ \frac{N!}{(N+2L+1)!(N+L+1)!} \right]^{\frac{1}{2}} . \tag{2.64}$$

For the angular parts we use the normal spherical harmonics. The Coulomb-Sturmians form a discrete and complete set in $L^2(\mathbb{R}^3)$ independent of the scaling parameter $\alpha > 0$ [40–43]. The hydrogen-like eigenfunctions can be recovered by replacing $\alpha \to a_{\text{exc}} n$ and thus the optimal value for $\alpha$ for a given state with $n_{\text{eff}}$ should scale roughly with $n_{\text{eff}}$. For the scaled system given in eq. (2.56) the convergence parameter $\alpha$ changes to the scaled convergence parameter

$$\tilde{\alpha} = \frac{\alpha}{n_{\text{eff}}^2}\,, \tag{2.65}$$

chosen such that the dimensionless coordinate $\rho$ in the radial part of the Coulomb-Sturmian functions (2.63) is not changing when transforming to scaled coordinates

$$\tilde{\rho} = \frac{\tilde{r}}{\tilde{\alpha}} = \frac{r}{n_{\text{eff}}^2} \frac{n_{\text{eff}}^2}{\alpha} = \rho\,. \tag{2.66}$$

Since the optimal value of $\alpha_{\text{opt}}$ scales roughly with $n_{\text{eff}}$ it follows for the scaled convergence parameter that

$$\tilde{\alpha}_{\text{opt}} = \frac{\alpha_{\text{opt}}}{n_{\text{eff}}^2} \propto \frac{1}{n_{\text{eff}}}\,, \tag{2.67}$$

and thus the optimal value is now smaller than one for the majority of the spectrum and decreases when states of increasing $n_{\text{eff}}$ are considered. In the following we will denote the convergence parameter as $\alpha$ for the unscaled and scaled system for reasons of simplicity.

We now use the ansatz

$$|\Psi\rangle = \sum_{N,L,J,F,M_F} c_{N,L,J,F,M_F} |\Pi\rangle\ , \tag{2.68}$$

with coefficients $c$. The functions (2.63) do not obey the orthogonality relations in $L^2(\mathbb{R}^3)$ [25]. With the overlap matrix

$$M_{\Pi'\Pi''} = \langle \Pi' | \Pi'' \rangle\ , \tag{2.69}$$

which is positive definite and symmetric[3] by definition, the completeness relation reads

$$1 = \sum_{\Pi'\Pi''} |\Pi'\rangle \, (M^{-1})_{\Pi'\Pi''} \, \langle\Pi''| \; . \tag{2.70}$$

Using the ansatz (2.68) we can write a generalized eigenvalue problem $A\,|\Psi\rangle = \lambda B\,|\Psi\rangle$ in matrix form by multiplying a basis state $\langle\tilde{\Pi}|$ from the left as

$$\begin{aligned} \langle\tilde{\Pi}|\, H\,|\Psi\rangle &= \lambda\,\langle\tilde{\Pi}|\, B\,|\Psi\rangle \;, \\ \sum_{\Pi} \langle\tilde{\Pi}|\, A\,|\Pi\rangle\, c_\Pi &= \lambda \sum_{\Pi} \langle\tilde{\Pi}|\, B\,|\Psi\rangle\, c_\Pi \;, \\ \sum_{\Pi} A_{\tilde{\Pi}\Pi} c_\Pi &= \lambda \sum_{\Pi} B_{\tilde{\Pi}\Pi} c_\Pi \;. \end{aligned}$$

For the Schrödinger equation $H\,|\Psi\rangle = \lambda\,|\Psi\rangle$ of the unscaled system with $\lambda = E$ the matrix elements $A_{\tilde{\Pi}\Pi}$ and $B_{\tilde{\Pi}\Pi}$ read

$$A_{\tilde{\Pi}\Pi'} = \langle\tilde{\Pi}|\, H\,|\Pi'\rangle \;, \qquad B_{\tilde{\Pi}\Pi} = M_{\Pi'\Pi''} \;. \tag{2.71}$$

For the generalized eigenvalue problem (2.56) of the scaled system with $\lambda = 1/n_{\text{eff}}^2$ the corresponding matrix elements read

$$A_{\tilde{\Pi}\Pi} = \langle\tilde{\Pi}|\, \tilde{H}\,|\Pi\rangle \;, \qquad B_{\tilde{\Pi}\Pi} = D_{\tilde{\Pi}\Pi} \equiv \langle\tilde{\Pi}|\, H_{\text{kin}}\,|\Pi\rangle \;. \tag{2.72}$$

Thus in both cases we have to solve a generalized eigenvalue problem

$$\boldsymbol{A}\boldsymbol{c} = \lambda \boldsymbol{B}\boldsymbol{c} \,, \tag{2.73}$$

with symmetric matrices [25] $\boldsymbol{A}$ and $\boldsymbol{B}$ and the latter being additionally positive definite as it is the overlap matrix (2.69) for the unscaled system and the matrix with elements $D_{\tilde{\Pi}\Pi}$ of the kinetic part (2.13) of the Hamiltonian (2.12) for the scaled one[4]. Further information about the matrix elements are given in [25] which have been converted to the matrix elements of the basis set (2.61) using Clebsch-Gordan coefficients.

As parity is a good quantum number [6], the generalized eigenvalue problem decomposes into two blocks with even and odd parity which corresponds to even and odd angular momentum $L$. Those blocks further decompose into four blocks because of the cubic symmetry of the kinetic part of the Hamiltonian $H_{\text{kin}}$ and the quantization axis chosen

[3] It is Hermitian and with the overlap $\langle\Pi'|\Pi''\rangle$ being real [25] it is symmetric.

[4] Intuitively the eigenvalues of the kinetic energy operator are always greater than zero due to the uncertainty principle which restricts the eigenfunctions to a finite extension in momentum space. Numerically this is confirmed by the algorithm used for solving the generalized eigenvalue problem where a positive definite matrix is needed.

parallel to one of the principal axis of the crystal [25]. More precisely, as a rotation of 90° about a four-fold symmetry axis of the group $O_\mathrm{h}$ does not change the Hamiltonian and one of those axis coincides with the quantization axis it follows

$$\begin{aligned}\langle\Pi'|\, e^{\frac{iF_z\pi/2}{\hbar}} H_\mathrm{kin} e^{\frac{-iF_z\pi/2}{\hbar}} \,|\Pi\rangle &= \langle\Pi'|\, e^{\frac{iM'_F\pi/2}{\hbar}} H_\mathrm{kin} e^{\frac{-iM_F\pi/2}{\hbar}} \,|\Pi\rangle \\ &= e^{\frac{i(M'_F-M_F)\pi/2}{\hbar}} \langle\Pi'|\, H_\mathrm{kin} \,|\Pi\rangle = \langle\Pi'|\, H_\mathrm{kin} \,|\Pi\rangle \ , \end{aligned} \tag{2.74}$$

where the last equation is only fulfilled if $M'_F - M_F = 4n$ with $n \in \mathbb{Z}$. Thus only states with $M_F = M'_F \mod 4$ couple. The four blocks correspond to the four equivalence classes of $M_F \mod 4$

$$[1/2] = \{\ldots, -15/2, -7/2, 1/2, 9/2, 17/2, \ldots\} \ , \tag{2.75}$$
$$[3/2] = \{\ldots, -13/2, -5/2, 3/2, 11/2, 19/2, \ldots\} \ , \tag{2.76}$$
$$[5/2] = \{\ldots, -11/2, -3/2, 5/2, 13/2, 21/2, \ldots\} \ , \tag{2.77}$$
$$[7/2] = \{\ldots, -9/2, -1/2, 7/2, 15/2, 23/2, \ldots\} \ . \tag{2.78}$$

With the symmetry plane orthogonal to the four-fould axis along the $z$-direction it follows that

$$\langle N', L', J', F', M'_F|\, H_\mathrm{kin} \,|N, L, J, F, M_F\rangle = \langle N', L', J', F', -M'_F|\, H_\mathrm{kin} \,|N, L, J, F, -M_F\rangle \ , \tag{2.79}$$

and thus for the matrices $\boldsymbol{D}$ defined in eq. (2.72)

$$\boldsymbol{D}_{M_F\in[1/2]} \sim \boldsymbol{D}_{M_F\in[7/2]} \ , \tag{2.80}$$
$$\boldsymbol{D}_{M_F\in[3/2]} \sim \boldsymbol{D}_{M_F\in[5/2]} \ , \tag{2.81}$$

where $\sim$ denotes similar matrices and thus their spectra are equal. They are similar because they can be transformed into each other by a basis transformation as only the arrangement of the basis vectors has to be changed. Thus the generalized eigenvalue problem (2.73) decomposes in both cases, the unscaled and scaled one, into four independent and different blocks, two for even and odd parity, respectively. This block structure is exploited to accelerate the diagonalization.

The symmetry of a state can be specified by the irreducible representations $\Gamma_i$ of the cubic $O_\mathrm{h}$ group which determine the transformation behaviour under symmetry operations of the group. When comparing the occurring eigenvalues in a given block with the assigned symmetries in ref. [7] the following structure is revealed. The blocks with $M_F \in [1/2]$ and $M_F \in [7/2]$ contain only eigenvalues corresponding to states with $\Gamma_7$ and $\Gamma_8$ symmetry. Likewise the blocks with $M_F \in [3/2]$ and $M_F \in [5/2]$ only contain $\Gamma_6$ and $\Gamma_8$ states. States with $\Gamma_6$ and $\Gamma_7$ symmetry are two-fold degenerate with one of the degenerate

states in each block they occur in. The $\Gamma_8$ states are four-fold degenerate and each of the four blocks contains one of the degenerate states. The block structure together with the degeneracies can thus be used to assign the symmetry of the exciton states corresponding to a given eigenvalue. We propose the following approach:

1. Label the eigenvalues by the block they occur in.
2. Merge the eigenvalues of two blocks with different spectra (e.g. the blocks with $M_F \in [1/2]$ and $M_F \in [3/2]$) and sort them in ascending order.
3. If two consecutive states are degenerate assign a $\Gamma_8$ symmetry.
4. Assign a $\Gamma_6$ or $\Gamma_7$ symmetry to the remaining states according to the block they belong to.

We numerically solve the generalized eigenvalue problem (2.73) with the LAPACK routine DSYGVX [44]. Thus one has to set bounds to the quantum numbers to get a finite basis set. In principle any set of $|N, L, J, F, M_F\rangle$ can be used to form a basis. As we use a hydrogen-like basis set and the Hamiltonian is also hydrogen-like perturbed by the valence band structure, we set an upper bound $n_{\max}$ to the principal quantum number $n$ to calculate spectra up to a certain $n_{\text{cal}} < n_{\max}$. By intuition the contribution of states with angular momentum $L \gtrsim n_{\text{cal}} - 1$ to the eigenfunctions with $n \leq n_{\text{cal}}$ should be small. This is indeed the case and thus we also set an upper bound $L_{\max}$ of the angular momentum $L$ to improve convergence by only accounting for the important contributions. As the convergence parameter $\alpha$ is the same for all basis functions our truncated basis set is uniquely defined by the triple $(\alpha, n_{\max}, L_{\max})$. As already mentioned above, our basis set is independent of the choice of the convergence parameter $\alpha$. However, for finite basis sets the approximation of a given eigenstate depends on the convergence parameter $\alpha$ and therefore it can be used to improve the approximation by an appropriate choice. This dependence decreases with an increasing basis size since more and more basis functions can correct for the errors of a given $\alpha$.

As we use a the finite basis set $(\alpha, n_{\max}, L_{\max})$ it is important to know how the eigenvalues relate to those of the infinite Hamilton matrix. The well-known variational principle

$$\frac{\langle\Psi|\, H\, |\Psi\rangle}{\langle\Psi|\Psi\rangle} \geq E_0\,, \tag{2.82}$$

gives a lower bound, namely the ground state energy $E_0$, to the eigenvalue of a trial function $|\Psi\rangle$. Arranging the eigenvalues in ascending order $E_0 \leq E_1 \leq \cdots$ and using a trial function $|\Psi_\perp\rangle$ which is orthogonal to the first $n$ eigenstates $\phi_i$ we get the generalized variational principle

$$\frac{\langle\Psi_\perp|\, H\, |\Psi_\perp\rangle}{\langle\Psi_\perp|\Psi_\perp\rangle} \geq E_n \quad \text{if } \langle\phi_i|\Psi_\perp\rangle = 0 \text{ for } i = 0, 1, \ldots, n-1\,. \tag{2.83}$$

Unfortunately eq. (2.83) is often not applicable as we would have to know the first $n$ exact eigenfunctions $|\psi_i\rangle$. There are exceptions, e.g. if we are interested in the lowest state of a representation of a known symmetry of the Hamiltonian, as then we can choose a trial function $|\Psi\rangle$ with the corresponding symmetry properties assuring orthogonality.

Fortunately there exists the following theorem which is of far more practical use [45]

**Theorem.** *Let* $|\psi_1\rangle, |\psi_2\rangle, \ldots, |\psi_N\rangle$ *be a set of orthonormal functions, and*

$$H_{nm} = \langle\psi_n| H |\psi_m\rangle \,, \tag{2.84}$$

*the resulting matrix elements of the Hamiltonian. Let* $\tilde{E}_s$ *be the eigenvalues of the* $N \times N$ *matrix thus defined, ordered in ascending order*

$$\tilde{E}_0 \leq \tilde{E}_1 \leq \cdots \leq \tilde{E}_{N-1} \,. \tag{2.85}$$

*Then each* $\tilde{E}_s$ *is an upper bound to the sth eigenvalue of the full Hamiltonian*

$$E_0 \leq \tilde{E}_0, \; E_1 \leq \tilde{E}_1, \; \ldots, \; E_{N-1} \leq \tilde{E}_{N-1} \,. \tag{2.86}$$

To prove this one can go the route over the Ritz-Galerkin projection and the Courant-Fischer min-max theorem as done in [46] or follow Peierls who found a simple and more transparent derivation [45]. Since a non-orthogonal basis set can be orthogonalized by a basis transformation (e.g. with the Löwdin orthogonalization) which does not change the eignevalues, the theorem also holds true for the generalized eigenvalue problem (2.73) for the unscaled system. Alternatively as the matrix $B$ on the r.h.s. of the generalized eigenvalue problem (2.73) is symmetric and positive definite the generalized eigenvalue problem can be transformed to a standard eigenvalue problem with the same eigenvalues [47]. From this it follows that also for the scaled system the theorem can be applied. To approximate the eigenvalues of the full system we thus have to systematically increase the basis size until they are converged, i.e. until the change of the former is below the desired precision. However this does not state in general which basis functions have the largest contributions to a given eigenfunction and thus the difficulty lies in finding an appropriate basis set that minimizes the dimension needed for convergence of the eigenvalues. It should also be noted that if one uses a basis set which excludes important basis functions independently of the basis size the eigenvalues will converge to a value above the true one. Thus it is essential on the one hand to choose basis functions from a complete basis to assure that the exact solution can be approximated arbitrarily close and on the other hand to not artificially exclude important basis functions, e.g. by choosing a too small $L_{\max}$ in our basis set $(\alpha, n_{\max}, L_{\max})$. Furthermore there are different optimal values for $\alpha$ for different eigenstates. Thus to get the best approximation to the real spectrum one has to perform calculations for a range of $\alpha$-values and merge the resulting spectra such that for each state the numerically smallest eigenvalue is taken. The convergence behavior of the eigenvalues is discussed in Appendix C.

### 2.3.2 Fourier transform of the density of states

As stated in section 2.2.2, Fourier transform (FT) of the scaled quantum density of states of eq. (2.56) should result in $\delta$-peaks at the scaled actions $\tilde{S}_{\mathrm{PO}}$ and their repetitions. This is only valid for an infinite spectrum. For the finite one, resulting from the diagonalization of the truncated generalized eigenvalue problem of eq. (2.56), the $\delta$-peaks are broadened and side peaks occur. This can be seen as follows. The FT of the finite spectrum corresponds to the FT of the infinite one multiplied by a rectangular window function. With the convolution theorem this is equivalent to a convolution of the Fourier transformed infinite spectrum with

$$\frac{\sin\left(\Delta n_{\mathrm{eff}}\tilde{S}_{\mathrm{po}}/2\right)}{\pi\tilde{S}_{\mathrm{po}}}e^{-in_{\mathrm{eff}}^{0}\tilde{S}_{\mathrm{po}}},$$

where $\Delta n_{\mathrm{eff}}$ is the size of the window, i.e. the length of the finite spectrum, and $n_{\mathrm{eff}}^{0}$ the center of the spectrum. To suppress the artificial side peaks a Gaussian window function $w(n_{\mathrm{eff}})$ is introduced

$$w(n_{\mathrm{eff}}) \equiv \exp\left(-\frac{(n_{\mathrm{eff}}-n_{\mathrm{eff}}^{0})^{2}}{2\sigma^{2}}\right),$$

with $\sigma = \Delta n_{\mathrm{eff}}/6$. Unfortunately this further broadens the main peaks. As the quantum spectrum is a sum of delta distributions the FT can be carried out analytically

$$\begin{aligned}\hat{\rho}(S) &= \frac{1}{2\pi}\sum_{k=1}^{k_{\max}}\int_{\mathbb{R}} w(n_{\mathrm{eff}})\delta(n_{\mathrm{eff}}-n_{\mathrm{eff},k})e^{-in_{\mathrm{eff}}S}\,\mathrm{d}n_{\mathrm{eff}}\\ &= \frac{1}{2\pi}\sum_{k=1}^{k_{\max}} w(n_{\mathrm{eff},k})\left[\cos(n_{\mathrm{eff},k}S) - i\sin(n_{\mathrm{eff},k}S)\right],\end{aligned} \tag{2.87}$$

where $k$ numerates the eigenvalues $n_{\mathrm{eff},k}$ from the first to the last $k_{\max}$ of the finite spectrum.

When using the Fourier transform to extract the amplitudes and actions of periodic orbits using eq. (2.48) from a finite quantum spectrum of length $\Delta n_{\mathrm{eff}}$ the resolution $\Delta S$ of the corresponding recurrence spectrum is proportional to the inverse of $\Delta n_{\mathrm{eff}}$. This property is often referred to as the uncertainty principle of the Fourier transform. It is thus impossible to resolve periodic orbits with separation of the actions smaller than $\Delta S$ as then the recurrence peaks overlap. With the occurrence of artificial side peaks, which have to be suppressed, a precise determination of the amplitudes is also not possible especially for overlapping peaks. To circumvent those problems the method of harmonic inversion [10, 11] can be applied which will be discussed in the next section. In this method the frequency space is not discretised on a grid with equally spaced points as for

example in the discrete Fourier transform. The grid points are them self free parameters leading to a non-linear problem.

### 2.3.3 High-resolution spectral analysis using the method of harmonic inversion

When the scaling technique of section 2.2.3 is applied the fluctuating part of the semi-classical trace formula can be written as (compare eq. (2.48))

$$\rho^{\mathrm{sc}}(n_{\mathrm{eff}}) = \sum_{\mathrm{PO}} \frac{1}{2} \left( A_{\mathrm{PO}} e^{i\tilde{S}_{\mathrm{PO}} n_{\mathrm{eff}}} + A^*_{\mathrm{PO}} e^{-i\tilde{S}_{\mathrm{PO}} n_{\mathrm{eff}}} \right) . \tag{2.88}$$

The key idea is now to adjust the quantum mechanical density of states eq. (2.58) to the functional form of eq. (2.88) with the amplitude and action forming a set of free in general complex adjusting parameters $\{A_{\mathrm{PO}}, \tilde{S}_{\mathrm{PO}}\}$. The procedure of extracting the parameters of the "harmonics" is why the method is referred to as *harmonic inversion*. For a numerical treatment we normally need to regularize the delta functions in (2.58) as the signal is needed on an equidistant grid. This could be done in principle by convolution with, e.g., a Gaussian function. In this thesis we will use a different approach introduced in [11] which consists of two steps: firstly only a window of actions is selected resulting naturally in a smooth signal and secondly the numerical extraction of the amplitudes and actions.

We follow ref. [11] but adjust the discussion to our problem of obtaining the recurrence spectrum. For the first step we Fourier transform the quantum mechanical density of states

$$\hat{\rho}^{\mathrm{qm}}(\tilde{S}) = \frac{1}{2\pi} \sum_k e^{-i\tilde{S} n_{\mathrm{eff},k}} , \tag{2.89}$$

and then apply a rectangular filter

$$f(\tilde{S}) = \begin{cases} 1 & \text{if } \tilde{S} \in [\tilde{S}_0 - \Delta\tilde{S}, \tilde{S}_0 + \Delta\tilde{S}] , \\ 0 & \text{else} , \end{cases} \tag{2.90}$$

thereby restricting the recurrence spectrum to only contributions within the window resulting in a band-limited signal. After applying the inverse Fourier transform we get the band-limited density of states

$$\begin{aligned} \rho^{\mathrm{qm}}_{\mathrm{bl}}(n_{\mathrm{eff}}) &= \frac{1}{2\pi} \sum_k \int_{\tilde{S}_0 - \Delta\tilde{S}}^{\tilde{S}_0 + \Delta\tilde{S}} e^{-i\tilde{S}_k n_{\mathrm{eff}}} e^{i n_{\mathrm{eff}} (\tilde{S} - \tilde{S}_0)} \, \mathrm{d}\tilde{S} \\ &= \sum_k \frac{\sin\left(\Delta\tilde{S}(n_{\mathrm{eff}} - {}_k n_{\mathrm{eff}})\right)}{\pi(n_{\mathrm{eff}} - {}_k n_{\mathrm{eff}})} e^{-i\tilde{S}_{0k} n_{\mathrm{eff}}} , \end{aligned} \tag{2.91}$$

thereby introducing a shift in the action domain by $-\tilde{S}_0$ which will be discussed below. The same procedure is applied to the semiclassical density of states eq. (2.88). The Fourier transform of eq. (2.88) reads

$$\hat{\rho}^{\mathrm{sc}}(\tilde{S}) = \frac{1}{2}\sum_{\mathrm{PO}} \left( A_{\mathrm{PO}}\delta(\tilde{S} - \tilde{S}_{\mathrm{PO}}) + A^*_{\mathrm{PO}}\delta(\tilde{S} + \tilde{S}_{\mathrm{PO}}) \right) . \tag{2.92}$$

Applying the rectangular filter (2.90) and restricting ourselves to the case where the window lies in the positive half space of the recurrence spectrum we get

$$\begin{aligned} \rho^{\mathrm{sc}}_{\mathrm{bl}}(n_{\mathrm{eff}}) &= \frac{1}{2}\sum_{\mathrm{PO}} \int_{\tilde{S}_0-\Delta\tilde{S}}^{\tilde{S}_0+\Delta\tilde{S}} \left( A_{\mathrm{PO}}\delta(\tilde{S} - \tilde{S}_{\mathrm{PO}}) + A^*_{\mathrm{PO}}\delta(\tilde{S} + \tilde{S}_{\mathrm{PO}}) \right) e^{in_{\mathrm{eff}}(\tilde{S}-\tilde{S}_0)}\, \mathrm{d}\tilde{S} \\ &= \frac{1}{2}\sum_{\mathrm{PO}} A_{\mathrm{PO}} e^{in_{\mathrm{eff}}(\tilde{S}_{\mathrm{PO}}-\tilde{S}_0)} \qquad \text{with } |\tilde{S}_{\mathrm{PO}} - \tilde{S}_0| < \Delta\tilde{S} \,. \end{aligned} \tag{2.93}$$

We now assume that the band-limited semiclassical density of states eq. (2.93) only consists of a finite number $K$ of actions, i.e. only a finite number of periodic orbits contribute to the signal. Adjusting the band-limited quantum signal (2.91) to the form of eq. (2.93) can then be written as a set of $2K$ non-linear equations

$$\rho^{\mathrm{qm}}_{\mathrm{bl}}(m\tau) \equiv c_m = \sum_{k=1}^{K} A_k e^{i\tilde{S}'_k m\tau} = \sum_{k=1}^{K} A_k z_k^m \,, \qquad m = 0, 1, \ldots, 2K-1 \,, \tag{2.94}$$

for the $2K$ unknown parameters which are the shifted actions $\tilde{S}'_k = \tilde{S}_{\mathrm{PO}} - \tilde{S}_0$ or the introduced parameter $z_k = \exp\left(i\tilde{S}'_k m\tau\right)$ and the amplitudes $A_k$. Note that we absorbed the factor $1/2$ into the amplitude, such that $A_k$ is half the amplitude of the corresponding periodic orbit defined in eq. (2.59) and (2.60), for the central and mixed regular chaotic orbits, respectively. The quantum signal eq. (2.91) is thus evaluated on an equidistant grid $n_{\mathrm{eff}} = m\tau$ with step size $\tau \equiv \pi/\Delta\tilde{S}$, which will be justified below. Assuming a relatively small number of periodic orbits in the signal ($K \sim 50 - 200$) and thus small number of equations, we can resort to the otherwise numerically unstable numerical technique of linear predictor to solve the system of non-linear equations [11]. Writing eq. (2.94) in matrix form formally for the signal points $c_{m+i}$ with $i = 1, \ldots, K$ reads

$$\boldsymbol{c}_m = \begin{pmatrix} c_{m+1} \\ \vdots \\ c_{m+K} \end{pmatrix} = \begin{pmatrix} z_1^{m+1} & \cdots & z_K^{m+1} \\ \vdots & & \ldots \\ z_1^{m+K} & \cdots & z_K^{m+K} \end{pmatrix} \begin{pmatrix} A_1 \\ \vdots \\ A_K \end{pmatrix} = \boldsymbol{Z}_m \boldsymbol{d} \,. \tag{2.95}$$

When multiplying from the left with the inverse matrix $\boldsymbol{Z}_m^{-1}$ we get the representation of the column vector $\boldsymbol{d} = \boldsymbol{Z}_m^{-1}\boldsymbol{c}_m$. Multiplying with the row vector $\boldsymbol{z}_m^t = (z_1^m \cdots z_K^m)$ from

the left we get

$$c_m = \boldsymbol{z}_m^t \boldsymbol{d} = \boldsymbol{z}_m^t \boldsymbol{Z}_m^{-1} \boldsymbol{c}_m = \boldsymbol{b}_m \boldsymbol{c}_m = \sum_{k=1}^{K} b_k c_{m+k} \,, \tag{2.96}$$

thus the signal points $c_m$ can be "predicted" by a linear combination of the following $K$ points where the coefficients $b_k$ are fixed. Those can be obtained as the solution of the resulting matrix equation when writing eq. (2.96) into matrix form for $m = 0, \ldots, K-1$

$$\begin{pmatrix} c_0 \\ \vdots \\ c_{K-1} \end{pmatrix} = \begin{pmatrix} c_1 & \cdots & c_K \\ \vdots & & \vdots \\ c_K & \cdots & c_{2K-1} \end{pmatrix} \begin{pmatrix} b_1 \\ \vdots \\ b_K \end{pmatrix} . \tag{2.97}$$

Having those at hand we can rewrite eq. (2.96) with the use of eq. (2.94) into

$$c_m = \sum_{k=1}^{K} b_k c_{m+k} = \sum_{k=1}^{K} \sum_{l=1}^{K} b_k A_l z_l^{m+k} \,. \tag{2.98}$$

Subtracting eq. (2.94) we thus get

$$\sum_{l=1}^{K} \left[ \sum_{k=1}^{K} b_k z_l^{m+k} - z_l^m \right] A_l = 0 \,, \tag{2.99}$$

which is fulfilled for arbitrary amplitudes $A_l$ if $z_l$ is a zero of the polynomial

$$\sum_{k=1}^{K} b_k z_l^k - 1 \,. \tag{2.100}$$

Having found the roots $z_k$ the amplitudes $A_k$ are obtained from the linear set of equations

$$c_m = \sum_{k=1}^{K} A_k z_k^m \,, \qquad n = 0, \ldots, K-1 \,. \tag{2.101}$$

The actions can be extracted by applying the complex logarithm

$$\tilde{S}'_k = -\frac{i}{\tau} \log(z_k) \,. \tag{2.102}$$

To circumvent the non-uniqueness of the complex logarithm we have introduced above the shift in the action domain by $-\tilde{S}_0$ such that $\tilde{S}' \in [-\Delta\tilde{S}, +\Delta\tilde{S}]$. For the argument of $z_k = \exp\left(i\tilde{S}'_k \tau\right)$ to be an element of $[-\pi, +\pi]$ the range of the filter eq. (2.90) has to satisfy

$$\Delta\tilde{S} = \frac{\pi}{\tau} \,. \tag{2.103}$$

This makes (2.102) unique and the actions $\tilde{S}_k = \tilde{S}_0 + \tilde{S}'_k$ can be extracted. When choosing a quantum spectrum of length $n_{\text{eff}}^{\max}$ [5] and thus a step width of

$$\tau = \frac{n_{\text{eff}}^{\max}}{2K}\,, \tag{2.104}$$

the action window has to fulfil eq. (2.103) such that

$$\Delta\tilde{S} = \frac{2\pi K}{n_{\text{eff}}^{\max}}\,. \tag{2.105}$$

Thus the quantum spectrum has to be long enough such that the number of periodic orbits in the range $[\tilde{S}_0 - \Delta\tilde{S}, \tilde{S}_0 + \Delta\tilde{S}]$ is less than $K$ and the set of amplitudes and actions $\{A_k, \tilde{S}_k\}$ converges. If this is the case not only the real periodic orbits but also spurious resonances are provided by harmonic inversion with low or near-zero amplitudes. They can be detected by a shift of the decimated signal. The spurious actions show large deviations with respect to the unshifted signal whereas the true actions usually coincide up to very high precision [11].

For solving the linear sets of equations (2.97) and (2.101) we resort to $LU$ decomposition. As the polynomial (2.100) can be rewritten into the characteristic polynomial of the so called Hessenberg matrix the roots are obtained by diagonalization of the latter [48]. We resort to this method as it is numerically more stable for polynomials of high order than other methods of root search [11].

[5] Also a window $[n_{\text{eff}}^{\min}, n_{\text{eff}}^{\max}]$ of the quantum spectrum can be chosen, but then the latter has to be shifted by $n_{\text{eff}}^{\min}$ such that the signal points $c_m$ and the position $n_{\text{eff}} = m\tau$ in eqs. (2.94) and (2.101) coincide. This introduces a phase factor of $\exp\left(in_{\text{eff}}^{\min}\tilde{S}'_k\right)$ which can be absorbed into the amplitude $A_k$ but of course has to be accounted for at the end of the calculation to obtain the true amplitude.

# 3 Results

In this chapter we present our results. In section 3.1 we first briefly discuss the quantum spectrum resulting for the unscaled Hamiltonian for comparison. We then discuss the quantum spectra of the scaled system for different values of $n_0$ and give a semiclassical interpretation of the corresponding recurrence spectra obtained by Fourier transform. In section 3.2 we then give a brief overview of the classical dynamics for excitons in cuprous oxide. For $n_0 = 5, 10$, and 15 we compare the quantum recurrence spectra obtained by Fourier transform to the semiclassical recurrence spectra in section 3.3. At last we do the same for the quantum recurrence spectrum obtained by harmonic inversion for $n_0 = 5$ and discuss the advantages and limitations of this method.

## 3.1 Quantum mechanical results

In fig. 3.1 a section of the spectrum of the unscaled Hamiltonian eq. (2.12) is shown, i.e. without applying the scaling technique to the system. Due to the band structure and the resulting mixing of the green and yellow series as well as the reduction to $O_\mathrm{h}$ symmetry a clear fine-structure splitting is visible. Without the band structure those would be degenerate hydrogen-like states. The states are shifted to lower $n_\mathrm{eff}$ resulting in a positive quantum defect $\delta$ introduced in eq. (2.15). This is also visible in fig. 3.2 where the quantum defects are plotted against the principal quantum number $n$. They converge to constant values for large $n$ which is the same behavior as stated in ref. [4]. Note that we used an exciton Rydberg constant (see eq. (2.6)) with effective mass

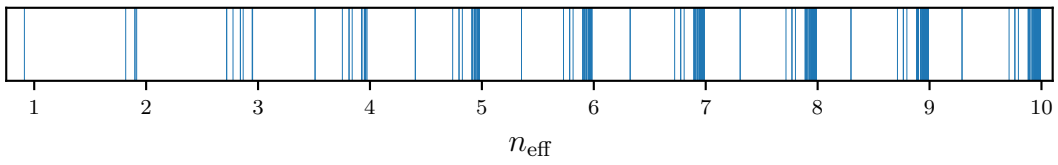


**Figure 3.1:** Spectrum of the unscaled Hamiltonian (2.12) over $n_\mathrm{eff}$. A clear splitting of the states around integer values of $n_\mathrm{eff}$ is visible.

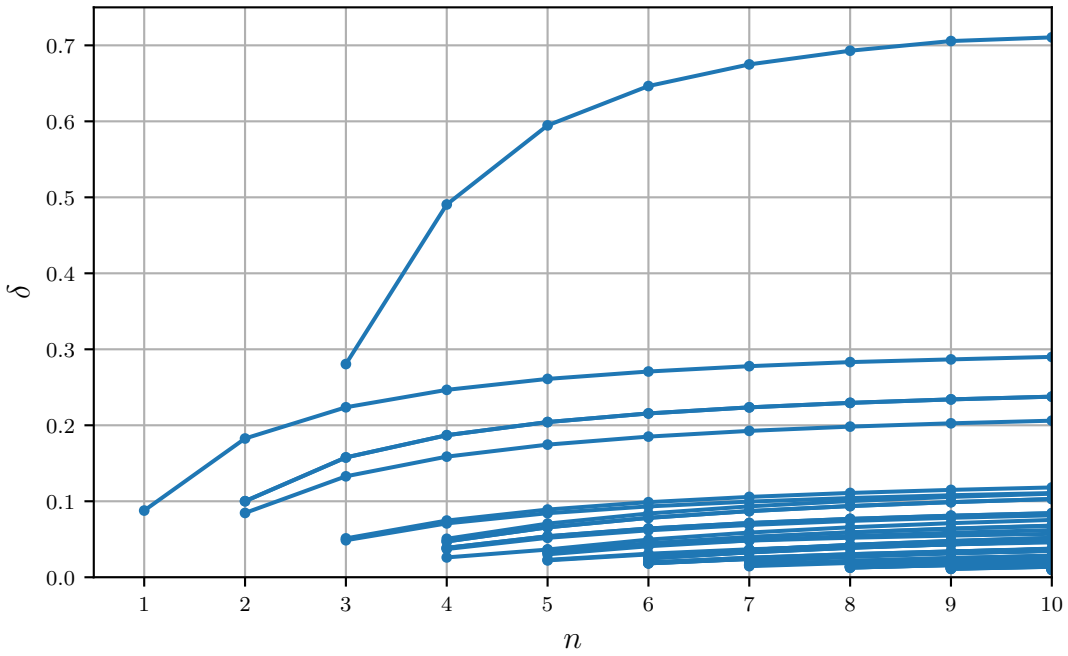


**Figure 3.2:** Quantum defects $\delta$ of the unscaled Hamiltonian (2.12) over the principal quantum number $n$.

$\mu = m_0/(\gamma_1' - 2\eta_1)$ adjusted to the yellow series when determining the eigenvalues $n_{\text{eff}}$ of the unscaled spectrum. For all other spectra we used an effective mass $\mu = m_0/\gamma_1'$. It should also be noted that the even parity states do not correspond to the physical ones of $Cu_2O$ as the central-cell corrections are not included (see section 2.1.2).

If we now introduce the energy-dependent spin-orbit coupling constant $\tilde{\Delta} = \frac{n_0^2}{n_{\text{eff}}^2}\Delta$ (see section 2.2.3) and thereby a classical scaling property to our system the spectrum gets dependent on the parameter $n_0$. As $\tilde{\Delta}$ determines the energy shift between the yellow and green series the two series get closer for increasing $n_{\text{eff}}$ and fixed $n_0$. $n_0$ determines the gradient with respect to $n_{\text{eff}}$, i.e. how fast the shift converges to zero for increasing $n_{\text{eff}}$. The influence of this parameter on the spectrum can be seen in fig. 3.3 where spectra for different values of $n_0$ are shown. The ratio of the scaled spin-orbit coupling constant $\tilde{\Delta}$ to the physical value $\Delta$ is given in the upper axis for each spectrum, respectively. In the vicinity of $n_{\text{eff}} = n_0$, i.e. $\tilde{\Delta}/\Delta = 1$, the physical and the scaled spectrum coincide locally. One can see an increasing influence of the green series to the spectrum for increasing $n_{\text{eff}}$ and fixed $n_0$ resulting in a more pronounced splitting of the states as well as a shift of the latter to lower values of $n_{\text{eff}}$. The same holds true if we follow the behavior of the states around integer values of $n_{\text{eff}}$ and decrease $n_0$.

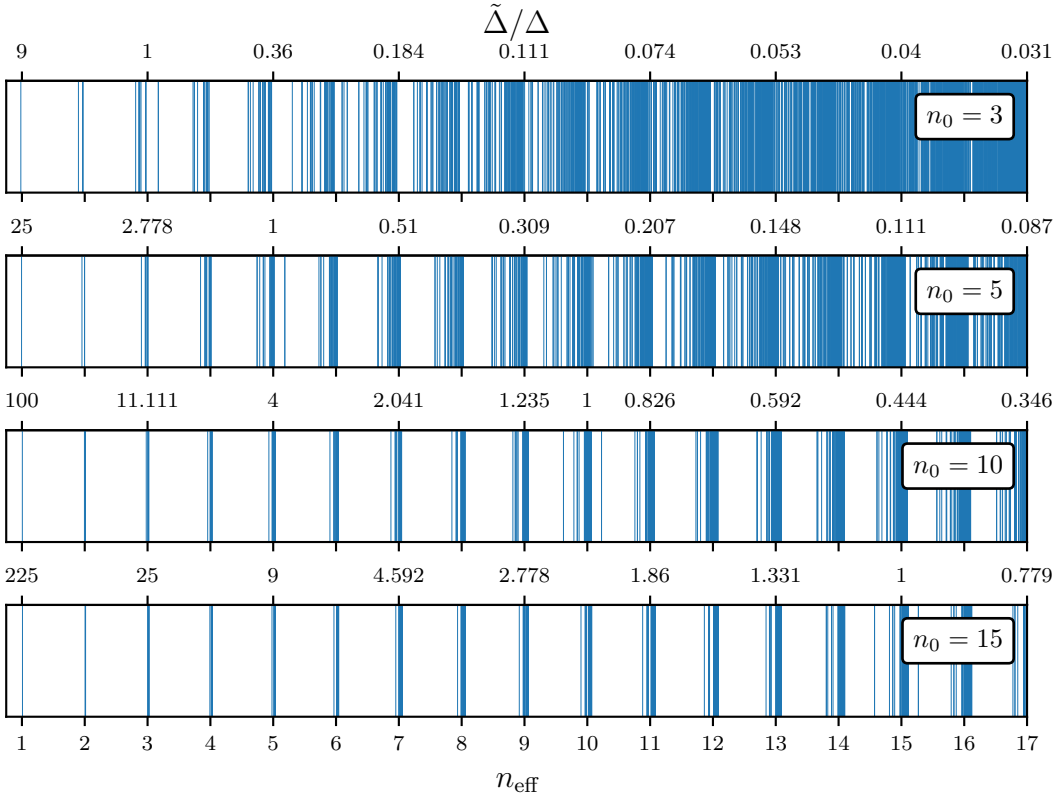


**Figure 3.3:** Spectra of the scaled system for different values of the parameter $n_0$. Already without the inclusion of the green series there exists a fine-structure splitting due to the cubic $O_\text{h}$ symmetry of the crystal. The influence of the green series is visible as a more pronounced fine-structure splitting which increases with increasing $n_\text{eff}$ for which the separation between the two series becomes smaller.

We Fourier transform quantum spectra up to $n_\text{eff}^\text{max} = 30$ with a Gaussian window function of width $\sigma = n_\text{eff}^\text{max}/6$ centered around $n_\text{eff}^\text{max}/2$ to suppress occurring side peaks (see section 2.3.2). In fig. 3.4 the absolute values of the resulting Fourier transformed spectra are plotted over $\tilde{S}/2\pi$ for different values of $n_0$. In figure 3.5 enlarged sections are shown. As discussed in section 2.2 the Fourier transformed spectrum can be interpreted semiclassical as the recurrence spectrum of periodic orbits of the associated classical mechanics. To emphasize the similarities and differences to the hydrogen-like case, where semiclassical peaks occur at multiples of $2\pi$ [49], we divide the scaled action $\tilde{S}$ by $2\pi$. One can see that it consists in general of sharp peaks with increasing density. Upon closer examination (see fig. 3.5) the following structures are visible. One can see how periodically occurring main peaks dominate the initial part. The latter increases for increasing values of $n_0$ ($\tilde{S}/2\pi \lesssim 4$ for $n_0 = 3$, $\tilde{S}/2\pi \lesssim 12$ for $n_0 = 5$, $\tilde{S}/2\pi \lesssim 50$ for $n_0 = 10$ and $\tilde{S}/2\pi \lesssim 113$ for $n_0 = 15$).

Also the amplitude of the main peaks increases with increasing $n_0$. The periodicity of the main peaks suggests that this part of the recurrence spectrum is dominated by one or a number of primitive periodic orbits with very similar action and their repetitions.

Going to higher values of $\tilde{S}$ the amplitude of those main peaks decreases more and more and simultaneously side peaks in between emerge which increase in their amplitude. Eventually the magnitude of the amplitudes of both the main and side peaks coincide. These transition regions are shown in fig. 3.5 for the different $n_0$ which span over an increasing action range for increasing $n_0$, note the broken action axes for $n_0 = 10$ and $n_0 = 15$.

The emergence of side peaks can be interpreted semiclassically as the occurrence of new periodic orbits with initially increasing contribution to the quantum density of states until it is comparable to the one of the periodic orbits forming the main peaks. For increasing action more and more side peaks emerge. As each new side peak corresponds semiclassically to a new primitive periodic orbit also peaks at multiples of their actions occur, i.e. multiple repetitions of the orbit, and the recurrence spectrum becomes more and more complex. This is particularly well visible for $n_0 = 3$ already at $\tilde{S}/2\pi \gtrsim 15$ in fig. 3.5.

## 3.2 Classical exciton dynamics

In this section we provide an overview of the classical exciton dynamics in $Cu_2O$ [50]. The periodic orbits of this dynamics will become important in the next section 3.3 where we use their contributions to the quantum spectra for a semiclassical interpretation of the latter.

The inclusion of the band structure with the use of energy surfaces $W_n$ (see section 2.1.3) leads to the reduction of the spherical symmetry $SO(4)$ of the hydrogen-like model to the cubic symmetry $O_\mathrm{h}$. The latter possesses nine symmetry planes of two kinds. Three planes perpendicular to the [001] axis and its equivalents and six planes perpendicular to the [011] axis and its equivalents. Those allow for a two-dimensional motion in the system, i.e. orbits in these symmetry planes. In contrast to the hydrogen-like case where only two-dimensional orbits are possible, also three-dimensional orbits exists. Examples of two- and fully three-dimensional orbits are shown in fig. 3.6. This leads to a rather complex phase space structure.

The six-dimensional phase space cannot be visualized directly. However the four-dimensional phase space of the two-dimensional orbits in the symmetry planes can be analyzed using a Poincaré surface of section (PSOS). For this a $(n-1)$-dimensional

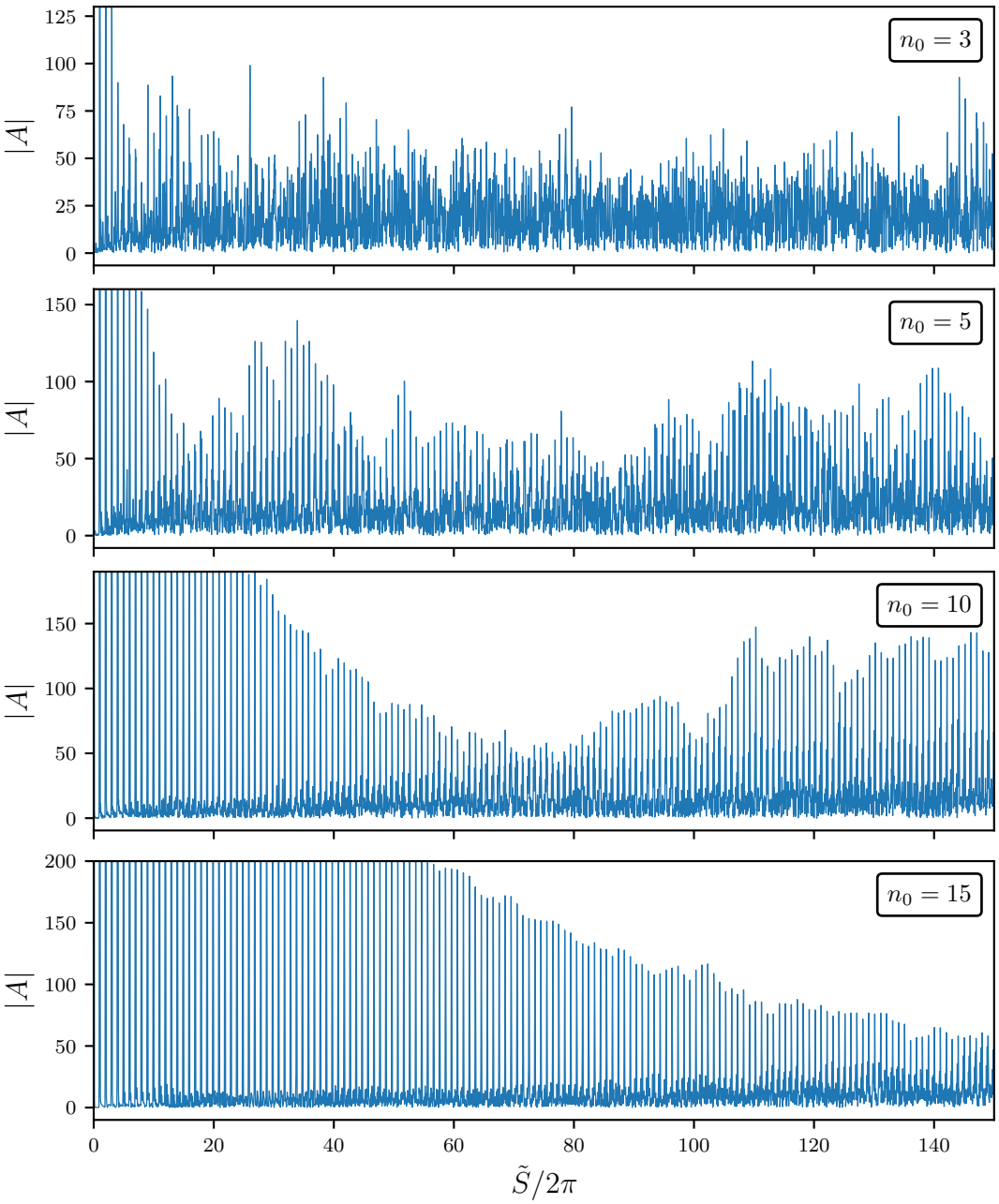


**Figure 3.4:** Absolute value of the Fourier transformed spectra for different $n_0$ which represents the quantum recurrence spectrum. Quantum spectra up to $n_{\text{eff}} = 30$ have been used and occurring side peaks have been suppressed by the use of a Gaussian window function.

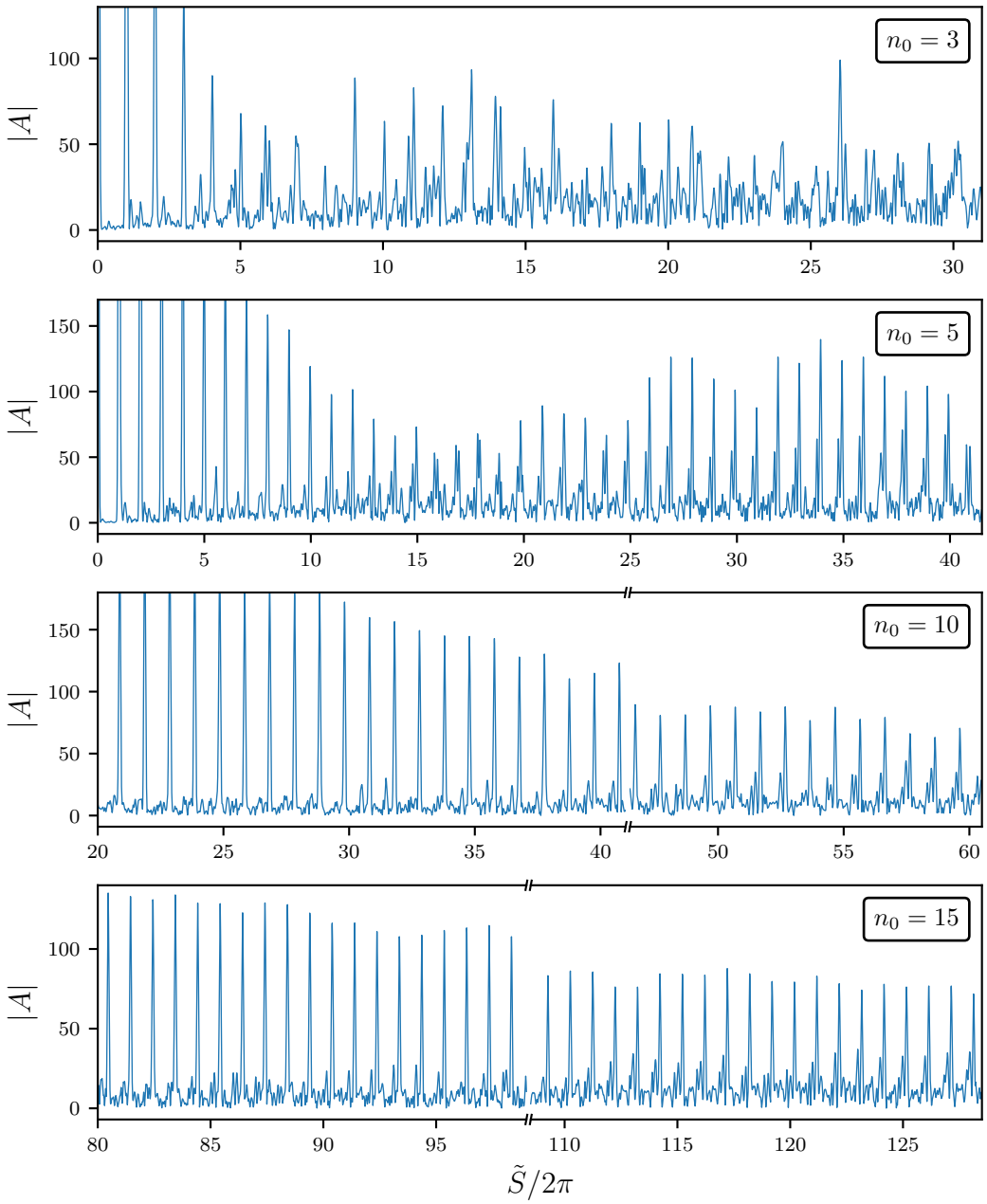


**Figure 3.5:** Enlarged sections of fig. 3.4 which show transition regions where the structure is changing. The initial part is dominated by equidistant main peaks. The structure changes when the amplitude of side peaks become comparable to the one of the main peaks. This happens at increasing values of $\tilde{S}/2\pi$ for increasing $n_0$. Therefore for $n_0 = 10$ and $n_0 = 15$ only the region of the onset of larger side peaks and the region where the order of magnitude of the amplitudes of the main and side peaks is similar are shown. The two regions are separated by a broken action axis.

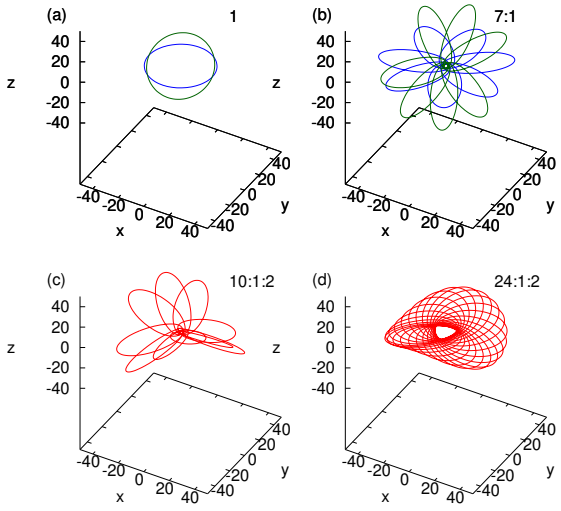


**Figure 3.6:** Examples of different types of orbits for $n_0 = 5$. (a) Nearly circular orbits with winding number $M_1 = 1$ and (b) planar orbits with winding numbers $M_1$:$M_2$ = 7:1 in the two different symmetry planes. (c) and (d): Two examples of fully three-dimensional orbits. The corresponding winding numbers are given in the top right. For the two- and three-dimensional orbits they are given as $M_1$:$M_2$ and $M_1$:$M_2$:$M_3$, respectively [50, 51].

hyperplane in the $n$-dimensional coordinate space is chosen. At intersection points with a trajectory the coordinates in the hyperplane are recorded and additionally the projection of the corresponding momenta onto it. The PSOS then consists of points at the recorded coordinates and momenta.

As all orbits in the symmetry planes orthogonal to the [001] and [101] axis pass through the $y$ axis we choose this axis as our one-dimensional hyperplane. It follows that the $x$ and $z$ coordinates are fixed to zero at the intersection points. Due to conservation of energy and the knowledge of $y$ and $p_y$ the momenta in $x$ and $z$ direction are also fixed as we know the orientation of the two-dimensional orbits in space. This leads to a two-dimensional PSOS with coordinates $(y, p_y)$. The other symmetry planes can be treated analogously. Periodic orbits lie in general on $D$-dimensional torus structures in phase space. The fixed points in the PSOS which correspond to periodic orbits also show these structures. Chaotic dynamics is visible as regions with a stochastic distribution of points. In fig. 3.7 such Poincaré surfaces of section for the plane perpendicular to the [001] axis are shown for different values of $n_0$. The coordinates $\tilde{x}_i = x_i/n_0^2$ and momenta $\tilde{p}_{x_i} = p_{x_i} n_0$ are scaled with $n_0$ (see discussion in section 2.2.3). The Poincaré surfaces of section show a change of the phase space structure when the energy corresponding to $n_0 = n_{\text{eff}}$ is varied. This is due to the fact that the system described by the Hamiltonian

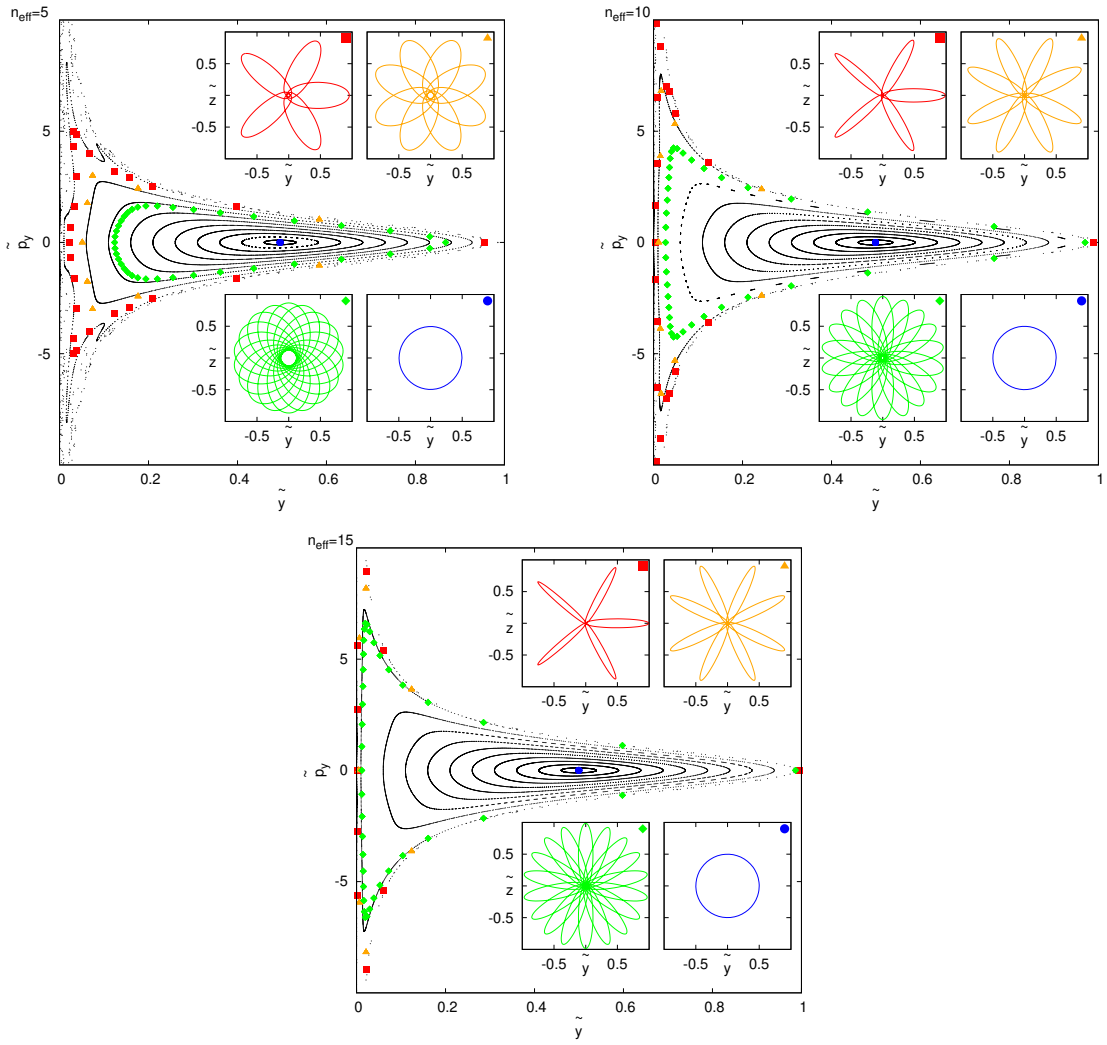


**Figure 3.7:** Poincaré surfaces of section for the orbits in the symmetry plane normal to [001] for increasing values of $n_0 = n_{\text{eff}}$ from left to right and top to bottom. Selected periodic orbits are shown in inserts and marked in the PSOS by corresponding symbols [50]. It is visible that the phase space structure is changing for different values of $n_{\text{eff}}$ corresponding to different energies.

(2.12) does not posses a classical scaling property as discussed in section 2.2.3.

The Poincaré surfaces of section consist of a central fixed point marked as a blue dot in fig. 3.7 which corresponds to a nearly circular orbit with the winding number $M_1$ counting its repetitions. This central fixed point is surrounded by regular tori. Also a small chaotic region is visible which shrinks for increasing $n_0$. The orbits corresponding to the regular tori are created by two fundamental motions, a motion along Kepler ellipses and a rotation of those around the origin, i.e. a secular motion. Thus they lie on two-dimensional tori and can be characterized by two winding numbers $M_i$. $M_1$ counts the number of Kepler ellipses and $M_2$ the number of cycles of the secular motion needed for a full cycle of the orbit. Starting from the outermost part of the PSOS and moving towards the central fixed point the ratio $M_1$:$M_2$ increases up to a maximum value $(M_1{:}M_2)_{\max}$ before the orbits are converged to the nearly circular orbit. The secular motion shows the influence of the symmetry reduction as the Runge-Lenz vector is not a conserved quantity anymore making such a motion possible. For increasing $n_0$ the maximum ratio $(M_1{:}M_2)_{\max}$ is also increasing which leads to a shift of the orbits with the same winding numbers towards the outermost part of the PSOS visible in fig. 3.7 and a deformation of the Kepler ellipses towards a line shape. An increasing value of $(M_1{:}M_2)_{\max}$ implies that the secular motion in the neighborhood of the central fixed points is slowing down resulting in a more hydrogen-like behavior in this region. For the symmetry plane perpendicular to [011] and equivalents $(M_1{:}M_2)_{\max}$ is larger than for the plane normal to [001] and equivalents. Therefore the former symmetry plane shows a more hydrogen-like behavior in the above mentioned region than the latter.

The three-dimensional orbits exhibit an additional secular motion out of the symmetry planes which can be characterized by a third winding number $M_3$. For $n_0 = 5$ two examples of such orbits can be seen in fig. 3.6.

## 3.3 Semiclassical interpretation of the quantum spectra

We now want to compare the quantum mechanical recurrence spectra with parameters $n_0 = 5, 10,$ and 15 to the corresponding semiclassical ones. This corresponds to a comparison of the quantum mechanics with the classical exciton dynamics at fixed energies $E = -1/2n_0^2$ corresponding to $n_0 = 5, 10,$ and 15. This is only reasonable for the scaled system where the classical dynamics is not changing over the spectrum. For the semiclassical recurrence spectrum J. Ertl [13] and M. Marquardt [14] extracted the scaled action $\tilde{S}$ and the orbit parameters needed to calculate the corresponding semiclassical amplitudes with eqs. (2.59) and (2.60), thus obtaining the position and amplitude in the

semiclassical recurrence spectrum. In figs. 3.8, 3.9, and 3.10 the quantum mechanical recurrence spectra for $n_0 = 5, 10$, and 15 are shown as a black solid line and the found semiclassical peaks as colored peaks with crosses at their end. The latter are also labeled by one to three winding numbers $M_i$ corresponding to the dimension of the tori the classical periodic orbits lie on in phase space (see section 3.2). Note that for $n_0 = 10$ and $n_0 = 15$ fully three-dimensional orbits are not shown[1]. As can be seen the quantum recurrence spectra resemble the semiclassical ones very well in the shown parts. The main peaks can be assigned to the contributions of planar nearly circular orbits in both symmetry planes and their repetitions with a corresponding single winding number $M_1$. For those nearly circular orbits the semiclassical amplitudes are larger for the orbits in the symmetry plane perpendicular to the [011] axis which shows a more hydrogen-like behavior (see section 3.2). The semiclassical peaks with the same winding number $M_1$ show an increasing amplitude and a small shift of their position towards smaller values of $\tilde{S}/2\pi$ when $n_0$ is increased. This coincides with the behavior of the quantum recurrence spectra. For $n_0 = 5$ they dominate the spectrum up to $\tilde{S}/2\pi \approx 12$ and for $n_0 = 10$ and $n_0 = 15$ the whole shown part. For the last two values of $n_0$ the main and side peaks have the same order of magnitude only at very high values of $\tilde{S}/2\pi$ as discussed in section 3.1. For $n_0 = 5$ the first side peak with a counterpart in the shown semiclassical recurrence spectrum appears at $\tilde{S}/2\pi \approx 5.6$ which can be assigned to the 5:1 planar orbit in the symmetry plane perpendicular to the [001] axis. Similarly for $n_0 = 10$ the first side peak can be assigned to the 7:1 and for $n_0 = 15$ to the 9:1 planar orbit in the same plane. Going to higher actions the appearing side peaks can be assigned to other two-dimensional planar orbits and fully three-dimensional orbits (only shown for $n_0 = 5$) with new winding number ratios $M_1$:$M_2$ and their repetitions, making the spectra more and more complex. For increasing values of $n_0$ the contribution of the two- and three-dimensional orbits decreases relative to the contribution of the nearly circular orbits at low actions $\tilde{S}/2\pi$. As they can be assigned to the side peaks this coincides with the behavior in the quantum recurrence spectrum. Orbits with small winding number ratio $M_1$:$M_2$ represent clear deviations to the hydrogen-like case as they exhibit a fast secular motion (see figs. 3.7 and 3.6) resulting from the perturbation of the hydrogen-like system by the band structure terms and the corresponding reduction to $O_\mathrm{h}$ symmetry.

Furthermore we can see for $n_0 = 5$ in fig. 3.8 that several semiclassical peaks with the same winding numbers $M_1$ and $M_2$ occur in clusters with very similar actions. In those clusters the peaks with the largest amplitude and action corresponds to planar orbits in the symmetry plane perpendicular to the [001] axis. Peaks which belong to fully three-dimensional orbits can be found at slightly smaller actions having also a smaller amplitude. Peaks corresponding to planar orbits in the symmetry plane perpendicular

[1] The calculation of those is much more complex and still a work in progress at the time of writing this thesis [50].

to the [011] axis are located at the lowest action within the cluster and also have the smallest amplitude. The same cluster structures are also visible for $n_0 = 10$ in fig. 3.9 and for $n_0 = 15$ in fig. 3.10 for the planar orbits in both symmetry planes. For increasing winding number ratios $M_1$:$M_2$ the clusters appear closer to the nearest main peaks with larger $\tilde{S}/2\pi$ values relative to the cluster. This is well visible in fig. 3.8 for $n_0 = 5$ but also for $n_0 = 10$ and $n_0 = 15$ in figs. 3.9 and 3.9, respectively. Furthermore it is visible that the clusters with the same winding number ratio $M_1$:$M_2$ are shifted to smaller actions $\tilde{S}/2\pi$ when $n_0$ is increased. With the finite resolution of the quantum recurrence spectrum the single peaks in clusters can not be resolved and appear as one common peak. This is well visible for the main peaks which consists of two central orbits, one in each symmetry plane. But also many single side peaks can be assigned to a number of semiclassical ones, for example to clusters with the same $M_1$ and $M_2$ winding numbers mentioned above.

To circumvent the finite resolution of the Fourier transform and also extract precise values for the semiclassical amplitudes we applied the method of harmonic inversion to the quantum spectrum with $n_0 = 5$ for which the most periodic orbits have been found so far. This method has been successfully applied in the past, for example to the hydrogen atom in an uniform magnetic field in ref. [10]. In fig. 3.11 the semiclassical recurrence spectrum together with the quantum one obtained by Fourier transform are shown again as in fig. 3.8 but now additionally with the peaks obtained using the harmonic inversion technique. We applied the method to the quantum spectrum up to $n_{\text{eff}} = 30$ and compared the resulting peaks with the ones obtained when the spectrum is shortened to $n_{\text{eff}} = 29$ to get an estimation of the convergence of the harmonic inversion. To only consider peaks which are converged comparably well we filtered those peaks with deviations in action smaller than $\Delta\tilde{S}/2\pi < 1 \times 10^{-2}$ and in amplitude $\Delta A$ smaller than 0.3 times the maximal amplitude of the two peaks compared. We also only show those which can be assigned to semiclassical ones for better visibility.

As can be seen in fig. 3.11 the overall agreement with the semiclassical peaks is good but not perfect. Especially the precise resolution of both the action and amplitude of all the single peaks in clusters is not possible as often only one peak has been found which can be assigned to one of the semiclassical peaks (see e.g. peak at $\tilde{S}/2\pi \approx 7$) or does not match in amplitude with any of the peaks (see e.g. peak at $\tilde{S}/2\pi \approx 15$). For the main peaks at $\tilde{S}/2\pi \approx 6$ and $\tilde{S}/2\pi \approx 10$ consisting of the two central orbits also two peaks had been found by harmonic inversion but only one peak has an amplitude comparable to one of the semiclassical peaks, respectively. Even for the semiclassical peaks which are well separated in action from the other ones there are deviations to the harmonic inversion peaks (see e.g. peak at $\tilde{S}/2\pi \approx 5.6$). Also not for all peaks appearing in the Fourier transform of the quantum spectrum which can be assigned to semiclassical peaks or cluster of peaks the harmonic inversion found corresponding converged ones. But

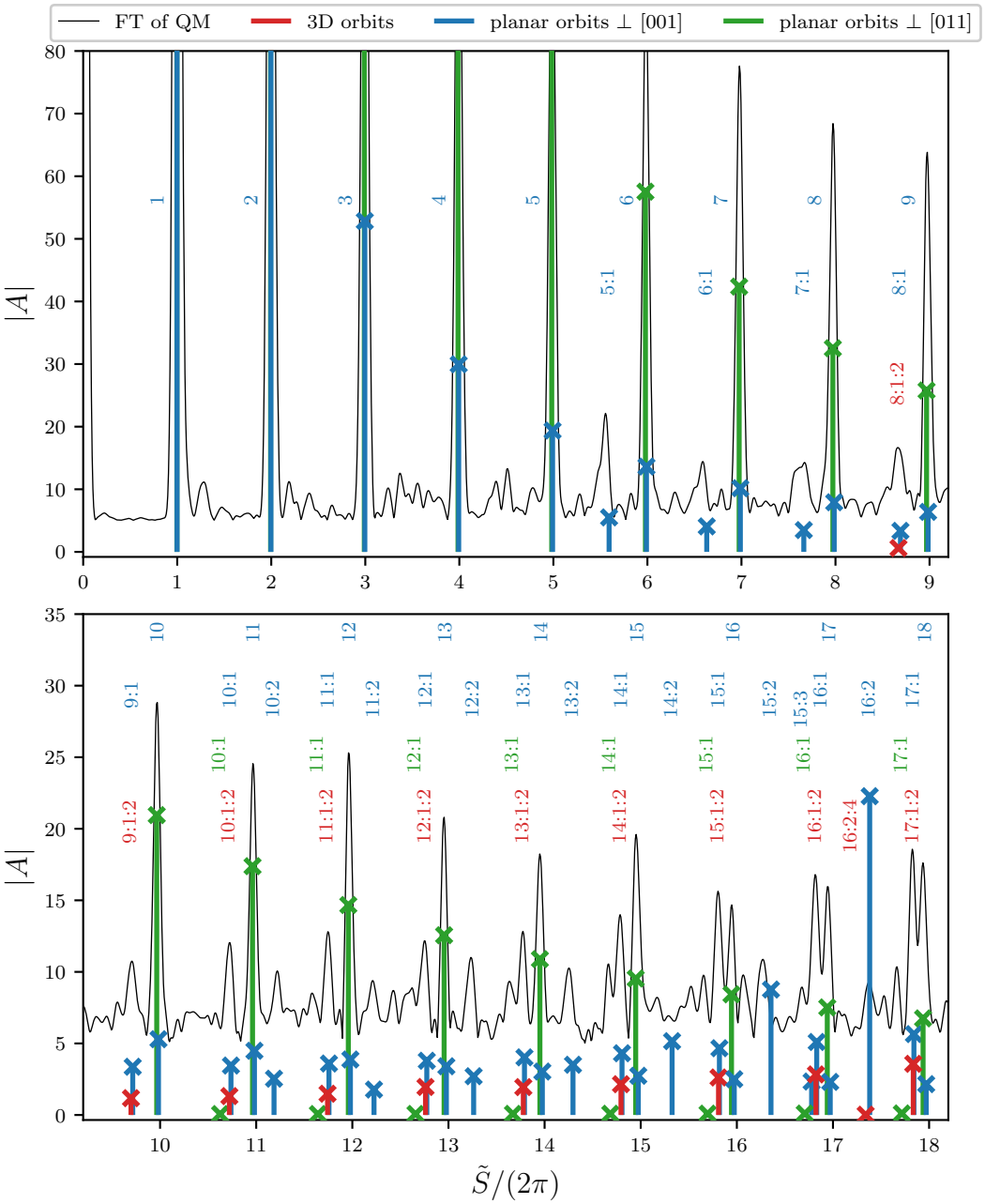


**Figure 3.8:** Quantum mechanical recurrence spectrum obtained by Fourier transform (FT) of the density of states (black solid line, with zero line shifted for better visibility) and the semiclassical recurrence spectrum (colored bars with cross at their end) resulting from periodic orbit parameters [14, 50] for $n_0 = 5$. The peaks are labeled with the corresponding winding numbers of the orbits. The nearly circular orbits with one winding number $M_1$, the planar orbits with two $M_1$:$M_2$ and the fully three-dimensional orbits with three $M_1$:$M_2$:$M_3$. Despite the restricted resolution of the quantum recurrence spectrum the observed structures agree very well with the semiclassical results.

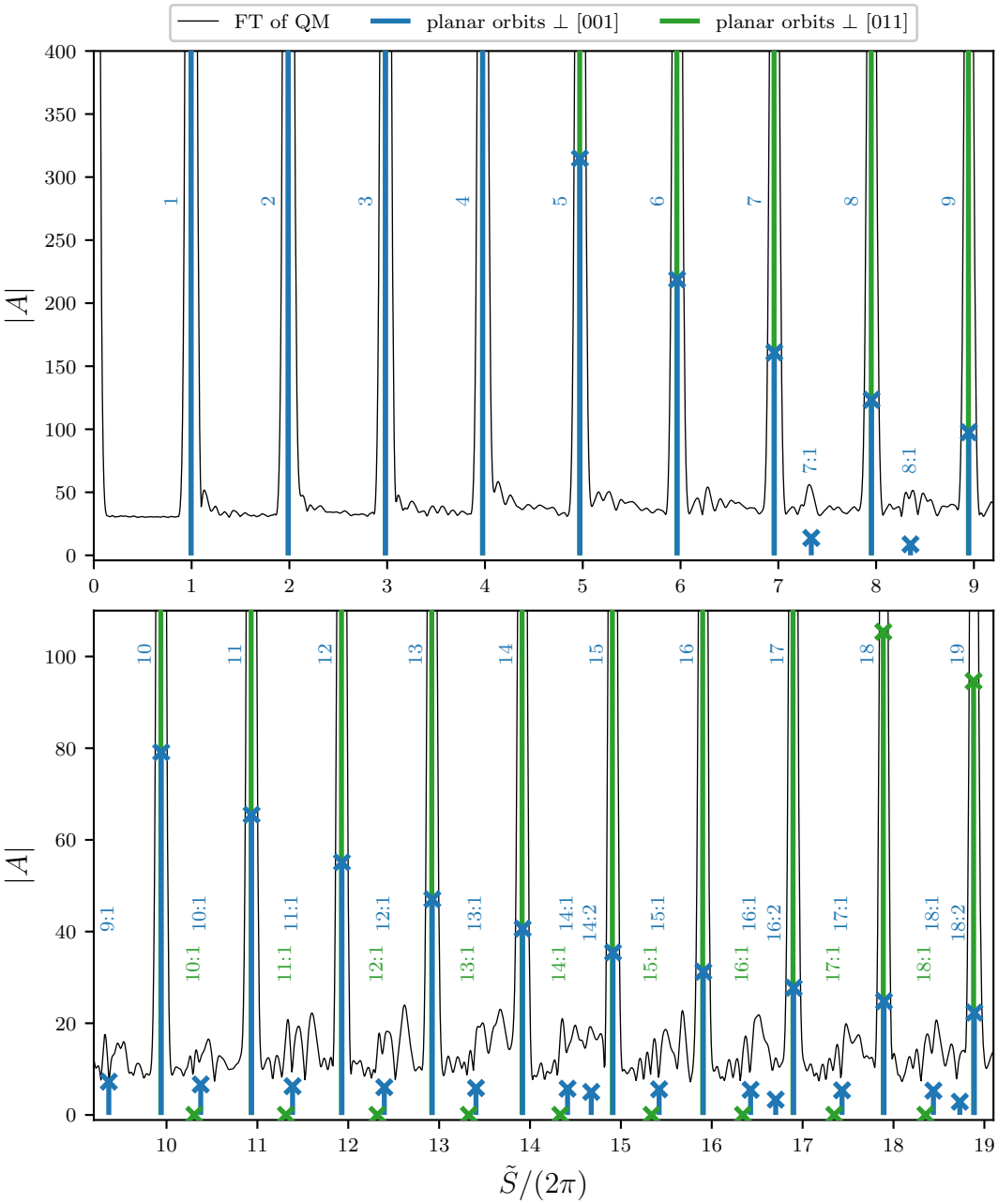


**Figure 3.9:** Same as fig. 3.8 but for $n_0 = 10$. Compared to the recurrence spectrum for $n_0 = 5$ in fig. 3.8 the peaks of the two-dimensional planar orbits with the same winding number ratio $M_1$:$M_2$ appear at smaller values of the action $\tilde{S}/2\pi$. Their amplitudes are also smaller relative to the ones of the nearly circular orbits. Furthermore the amplitudes of the peaks of the nearly circular orbits with the same winding number $M_1$ are larger and their positions are slightly shifted to smaller values of $\tilde{S}/2\pi$. This shift is better visible for larger $M_1$.

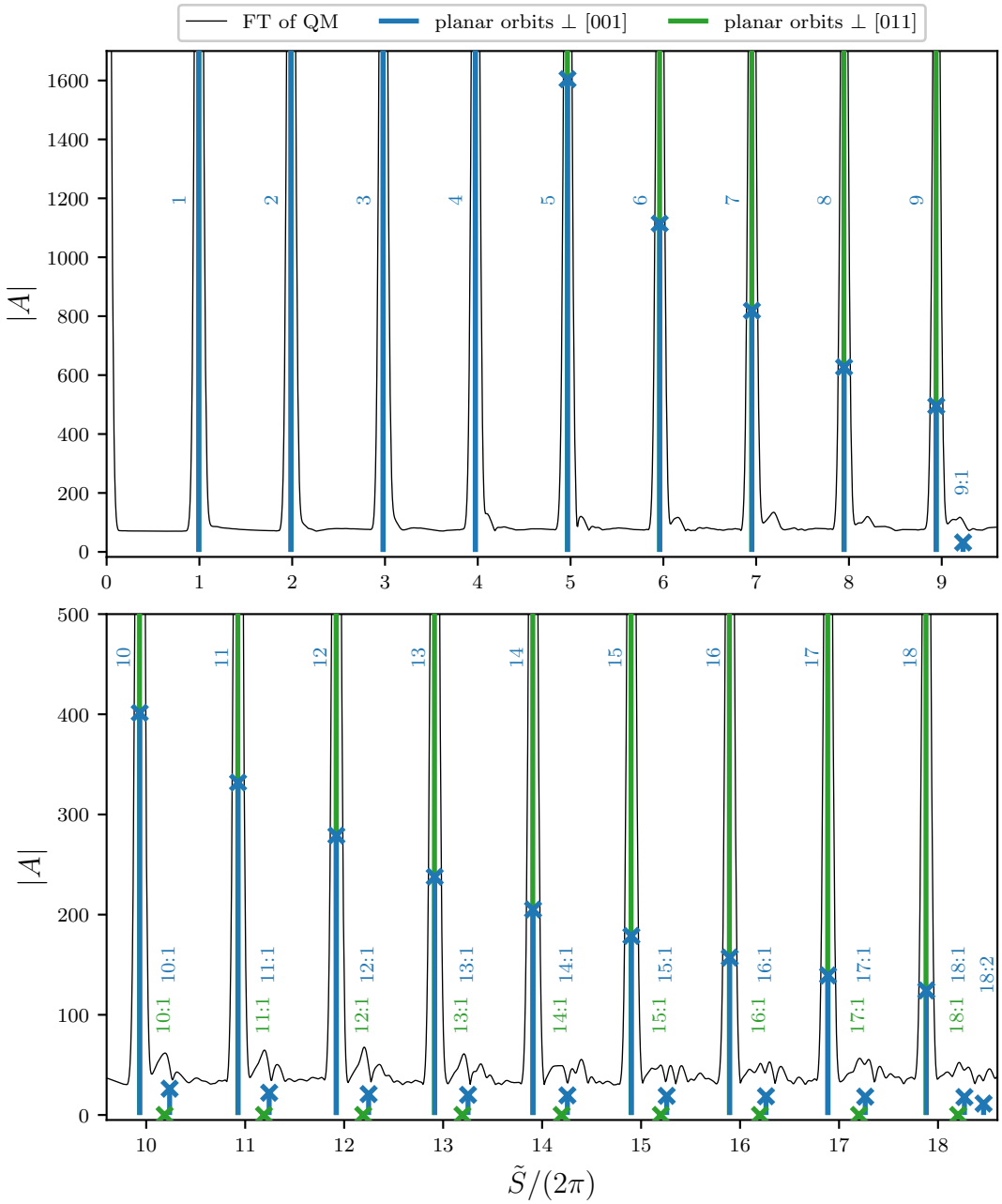


**Figure 3.10:** Same as fig. 3.8 but for $n_0 = 15$. Compared to the recurrence spectra for $n_0 = 5$ in fig. 3.8 and $n_0 = 10$ in fig. 3.9 the peaks of the two-dimensional planar orbits with the same winding number ratio $M_1$:$M_2$ appear at even smaller values of the action $\tilde{S}/2\pi$. Also their amplitudes are even smaller relative to the ones of the nearly circular orbits. Furthermore the amplitudes of the peaks of the nearly circular orbits with the same winding number $M_1$ are even larger and their positions are further slightly shifted to smaller values of $\tilde{S}/2\pi$. This shift is better visible for larger $M_1$.

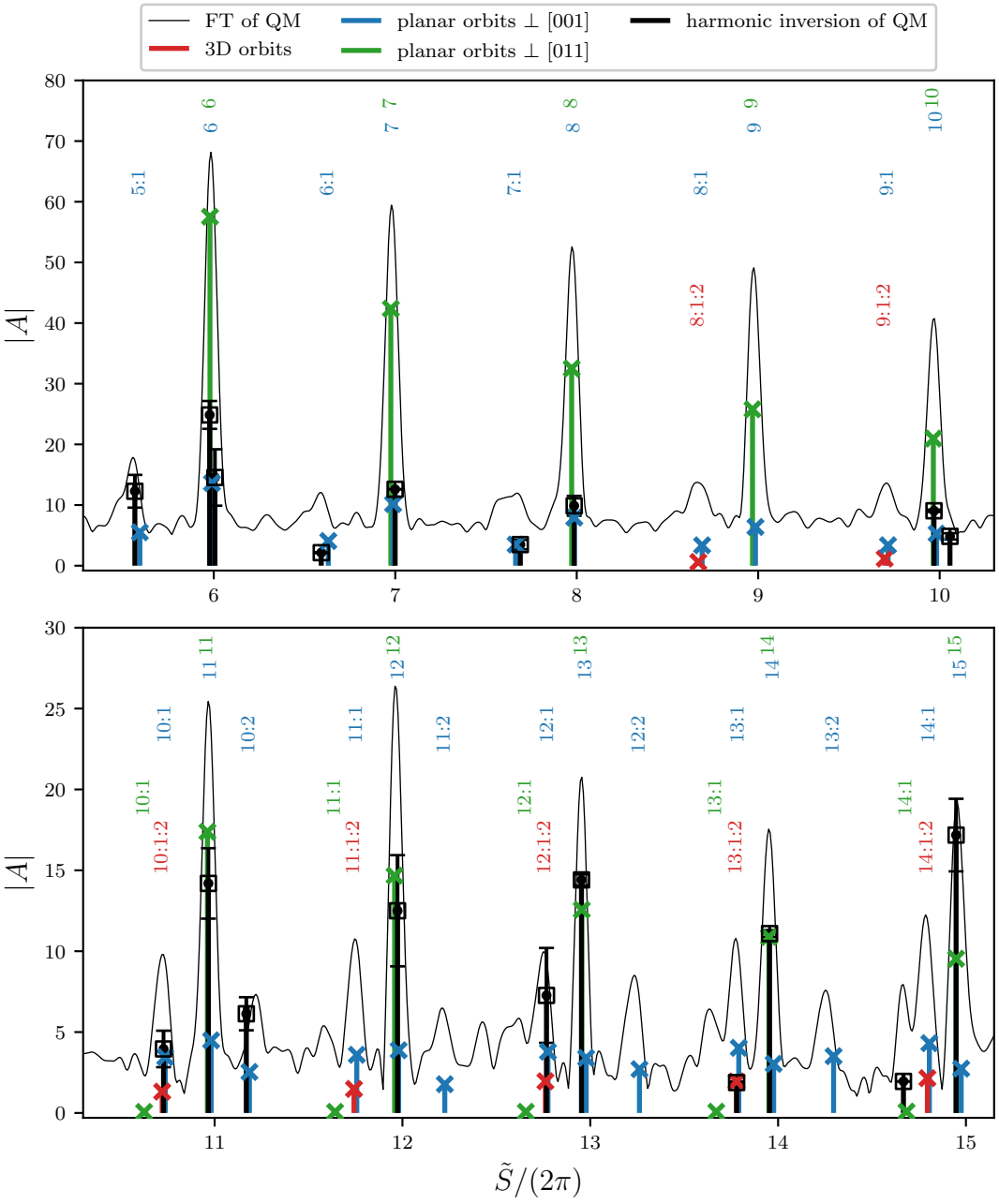


**Figure 3.11:** The quantum mechanical recurrence spectrum obtained via Fourier transform (FT) and the semiclassical peaks as in fig. 3.8 for $n_0 = 5$. Additionally peaks obtained by harmonic inversion are shown as black bars with open squares at their end. Only those which can be assigned to semiclassical ones are shown for better visibility. The error bars indicate the deviation when using a shorter quantum spectrum.

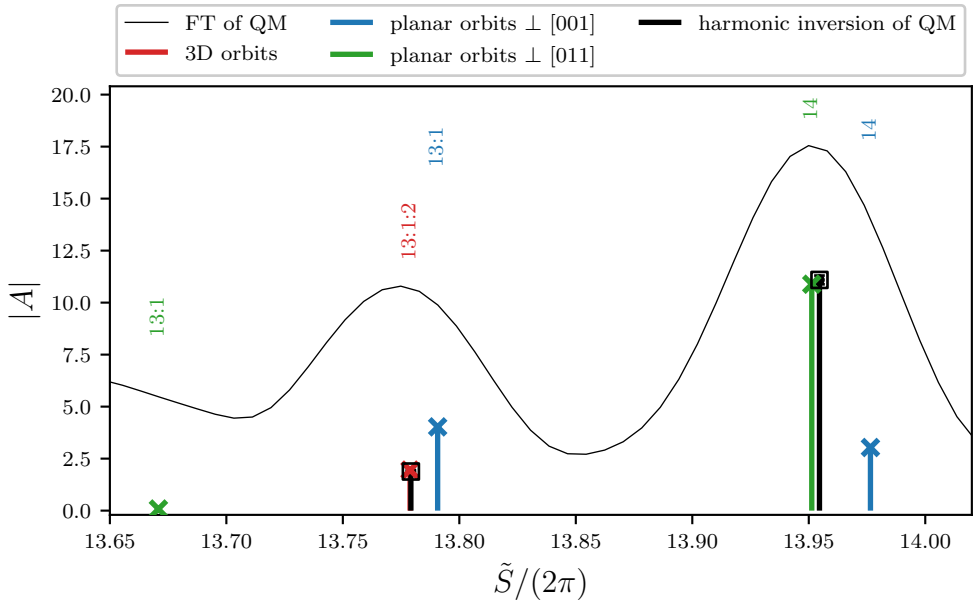


**Figure 3.12:** Enlarged region around $\tilde{S}/2\pi \approx 14$ of fig. 3.11.

there are cases where the agreement is relatively good. For example for the amplitude of the peak at $\tilde{S}/2\pi \approx 7.7$ or for both amplitudes and actions of the two peaks around $\tilde{S}/2\pi \approx 14$ as can be seen in fig. 3.12 where the environment of those is shown enlarged. Also the deviations $\Delta A$ and $\Delta\tilde{S}$ are rather small for those peaks resulting in the error bars being within the size of the open squares. Furthermore at least the magnitudes of most of the harmonic inversion and semiclassical peaks coincide. The deviations $\Delta A$ are also very different indicating a not uniform convergence. We give in table 3.1 the parameters for peaks with comparably good agreement. The relatively large imaginary parts of the actions of the harmonic inversion peaks, which should be purely real, are another indication for the harmonic inversion not being sufficiently converged.

The discussion above suggests that we would need a much larger quantum spectrum to achieve convergence of the harmonic inversion in more sections of the recurrence spectrum and thus be able to precisely determine the parameters of recurrence peaks for more than a few. Especially the clusters of semiclassical peaks where the actions are very similar result in beat-like structures in the density of states which are only resolvable if the latter is sufficiently large. Furthermore as the quantum spectrum consists of both the yellow and green series, and we only compare to classical periodic orbits of the yellow series, the green states can be regarded as noise which could also lead to a negative impact. Also the adiabatic approximation used in the classical calculation of the orbits could be an explanation for deviations between the quantum and semiclassical recurrence spectrum.

**Table 3.1:** Comparison between semiclassical peaks and peaks obtained by harmonic inversion for $n_0 = 5$. Here $\tilde{S}^{\mathrm{cl}}$ and $|A^{\mathrm{cl}}|$ denote the classical action and absolute amplitude, $\tilde{S}^{\mathrm{qm}}$ and $|A^{\mathrm{qm}}|$ the action and absolute amplitude obtained by harmonic inversion. In the first column, denoted as type, the axis normal to the symmetry plane of the classical orbit is given or whether it is fully three-dimensional. In the second column the winding numbers of the orbit is given in the sequence $M_1$:$M_2$:$M_3$. For the central orbits one winding number is given, for the two-dimensional orbits two, and for fully three-dimensional orbits three.

| Type | $M_1$:$M_2$:$M_3$ | $\tilde{S}^{\mathrm{cl}}/2\pi$ | $\mathrm{Re}(\tilde{S}^{\mathrm{qm}}/2\pi)$ | $\mathrm{Im}(\tilde{S}^{\mathrm{qm}}/2\pi)$ | $\lvert A^{\mathrm{cl}}\rvert$ | $\lvert A^{\mathrm{qm}}\rvert$ |
|---|---|---|---|---|---|---|
| 001 | 7:1 | 7.66318 | 7.68899 | 0.00886 | 3.48338 | 3.48060 |
| 011 | 13 | 12.95477 | 12.95324 | 0.00808 | 12.55954 | 14.40922 |
| 3D | 13:1:2 | 13.77886 | 13.77921 | 0.02033 | 1.94825 | 1.88011 |
| 011 | 14 | 13.95129 | 13.95459 | 0.00858 | 10.88491 | 11.09087 |
| 001 | 20:2 | 21.47462 | 21.53141 | 0.00095 | 5.87543 | 5.93607 |
| 001 | 22:3 | 24.01863 | 24.03714 | 0.01247 | 2.22511 | 1.63889 |
| 001 | 25:1 | 25.90233 | 25.89540 | 0.00496 | 25.81694 | 27.98979 |
| 001 | 24:4 | 26.52386 | 26.49738 | 0.00715 | 2.20162 | 1.96693 |
| 001 | 27:1 | 27.91121 | 27.90184 | 0.00933 | 20.23884 | 20.26489 |
| 001 | 32:4 | 34.76402 | 34.76036 | 0.01104 | 7.92119 | 8.59425 |
| 001 | 45:2 | 46.77631 | 46.76831 | 0.01270 | 6.04839 | 5.89007 |
| 001 | 46:2 | 47.78257 | 47.77200 | 0.00224 | 7.63200 | 11.61153 |
| 001 | 52:5 | 55.72697 | 55.74803 | 0.01347 | 5.10610 | 6.55482 |
| 001 | 57 | 56.90422 | 56.91011 | 0.00983 | 3.78123 | 4.06931 |
| 001 | 74:5 | 78.08051 | 78.08168 | 0.02037 | 1.64425 | 1.16820 |
| 001 | 75:4 | 78.43711 | 78.42513 | 0.01336 | 2.44305 | 1.60926 |
| 001 | 75:5 | 79.09337 | 79.09332 | 0.00568 | 1.68636 | 2.94249 |

# 4 Conclusion and outlook

We calculated quantum spectra of excitons in cuprous oxide including the complex band structure. To be able to directly identify contributions of periodic orbits of the associated classical dynamics at fixed energy, we applied a scaling technique to the quantum system. Those contributions could then be revealed by Fourier transform of the scaled quantum spectra to the corresponding recurrence spectra which exhibit peaks at the positions of the action of classical periodic orbits. This connection is established by semiclassical theories.

For the scaling of the system we appropriately replaced the spin-orbit coupling constant $\Delta$ determining the separation of yellow and green series by a scaled version $\tilde{\Delta} = \Delta n_0^2/n_{\text{eff}}^2$ depending on a parameter $n_0$, determining the energy of the associated classical dynamics. This results in a decreasing separation of the series for higher levels in the $n_{\text{eff}}$ spectrum and the associated classical dynamics stay the same over the whole quantum spectrum. As a consequence the corresponding spectra show an increasing fine-structure splitting when going to higher $n_{\text{eff}}$ levels. The strength of the splitting is also dependent on the choice of the parameter $n_0$.

The corresponding recurrence spectra exhibit peaks with increasing density as a function of the action. The structure can be described as follows. For small values of the action equidistant main peaks dominate the spectrum. Their amplitude decreases for increasing action and new peaks of increasing amplitude appear between those until their amplitude is comparable to the one of the main peaks. The size of the action range dominated by the main peaks depends on the parameter $n_0$ and is larger for a less pronounced fine-structure splitting in the quantum spectrum.

A comparison of the quantum and semiclassical recurrence spectra for $n_0 = 5$, $n_0 = 10$, and $n_0 = 15$ revealed the contributing classical periodic orbits. The main peaks could be assigned to two-dimensional nearly circular orbits in the symmetry planes of the crystal and the side peaks to more complex orbits with secular motion including two- and also fully three-dimensional orbits. This provides a deeper insight in the associated classical dynamics connected to the fine-structure splitting in $Cu_2O$. Because of the finite resolution of the Fourier transform and semiclassical peaks occurring in clusters with very similar actions there exist many peaks in the quantum recurrence spectrum to which

more than one periodic orbit can be assigned. To circumvent the finite resolution of the Fourier transformation and precisely determine the position and the amplitude of the semiclassical peaks we applied the method of harmonic inversion to the quantum spectrum. The attempt was successful for several peaks, however, the short quantum spectra in general do not allow us to fully resolve the clusters of peaks in the semiclassical recurrence spectrum.

Future work should concentrate on the calculation of scaled quantum spectra up to much higher energy levels. To reduce the numerical effort needed one could use a symmetry-adapted basis set to exploit the block structure of the Hamiltonian generated by the irreducible representations of the point group $O_h$. This would further reduce the dimension of the generalized eigenvalue problems we have to solve. Using a larger spectrum it should be possible to successfully apply the method of harmonic inversion and resolve the clusters of peaks present in the semiclassical recurrence spectra. This would enable one to precisely determine the action and amplitude of periodic orbit contributions to the quantum spectrum. If this is achieved one could extend the semiclassical analysis to more values of $n_0$ and thus consider the classical dynamics at different energies. Comparison of the corresponding recurrence spectra could then be used to determine the energy range for which the classical description is a good approximation. Where this is the case, we can gain a more complete insight into the associated classical physics. It will also be interesting to apply the semiclassical analysis of quantum spectra to other systems like magnetoexcitons in curpous oxide or even other materials.

# A Material parameters of cuprous oxide

The material parameters used in this thesis are listed in table A.1. The Luttinger parameters $\gamma_i$ and $\eta_i$ are obtained from the parameters $A_i$ and $B_i$ as [25]

$$\gamma_1 = -A_1\,, \qquad \gamma_2 = \frac{A_2}{6}\,, \qquad \gamma_3 = \frac{A_3}{6}\,,$$
$$\eta_1 = -B_1\,, \qquad \eta_2 = \frac{B_2}{6}\,, \qquad \eta_3 = \frac{B_3}{6}\,.$$

**Table A.1:** Material parameters of cuprous oxide used in this thesis.

| | | | |
|---|---|---|---|
| band gap energy | $E_g$ | 2.17208 eV | [2] |
| electron mass | $m_e$ | $0.99m_0$ | [52] |
| dielectric constant | $\varepsilon$ | 7.5 | [53] |
| spin-orbit coupling | $\Delta$ | 0.131 eV | [5] |
| valence band parameters | $A_1$ | -1.76 | [5] |
| | $A_2$ | 4.519 | [5] |
| | $A_3$ | -2.201 | [5] |
| | $B_1$ | 0.02 | [5] |
| | $B_2$ | -0.022 | [5] |
| | $B_3$ | -0.202 | [5] |

# B Exciton Hartree units

Units often used in atomic physics are the Hartree atomic units obtained by setting the unit charge $e$, free electron mass $m_0$, reduced Planck constant $\hbar$, and the Bohr radius $a_0$ to one. In analogy we use exciton Hartree units [25] by setting

$$\hbar = e = \frac{m_0}{\gamma_1'} = 4\pi\varepsilon_0\varepsilon = 1\,. \tag{B.1}$$

The unit length corresponds to the exciton Bohr radius

$$a_{\mathrm{exc}} = a_0\varepsilon\gamma_1' = \frac{4\pi\varepsilon_0\varepsilon\hbar^2\gamma_1'}{m_0e^2}\,, \tag{B.2}$$

and the energy unit is connected to the exciton $Ry^{\mathrm{exc}}$ and Rydberg constant $Ry$ of the hydrogen atom

$$E_{\mathrm{exc}} = 2Ry^{\mathrm{exc}} = 2\frac{Ry}{\gamma_1'\varepsilon^2} = \frac{\hbar^2\gamma_1'}{a_{\mathrm{exc}}^2 m_0}\,. \tag{B.3}$$

In table B.1 conversions to SI units are given for the parameters $\gamma_1' = 2.77$ and $\varepsilon = 7.5$.

**Table B.1:** Conversion factors from exciton Hartree to SI units.

| quantity | symbol | exc. Hartree unit | SI |
|---|---|---|---|
| charge | $q$ | $e$ | $1.602 \times 10^{-19}$ C |
| mass | $m$ | $m_0/\gamma_1'$ | $3.288 \times 10^{-31}$ kg |
| action | $S$ | $\hbar$ | $1.055 \times 10^{-34}$ Js |
| length | $r$ | $a_{\mathrm{exc}}$ | $1.099 \times 10^{-9}$ m |
| momentum | $p$ | $\hbar/a_{\mathrm{exc}}$ | $9.593 \times 10^{-26}$ kg m s$^{-1}$ |
| energy | $E$ | $E_{\mathrm{exc}}$ | $1.399 \times 10^{-20}$ J |
| time | $t$ | $\hbar/E_{\mathrm{exc}}$ | $3.769 \times 10^{-15}$ s |

# C Convergence behavior of the eigenvalues

Here we discuss the behavior of the eigenvalues for different choices of basis sets. If not otherwise stated we will refer to the scaled system (see section 2.2.3) with $n_0 = 5$. For other values of $n_0$ the behavior is similar. As mentioned in section 2.3.1 for a finite basis set the eigenfunctions become dependent on the convergence parameter $\alpha$ and thus also the eigenvalues. The typical behavior of the deviations $\varepsilon$ to the optimal eigenvalues for a range of different values of the convergence parameter can be seen in fig. C.1. It is visible that $\varepsilon$ is more sensitive to a change to larger values of $1/\tilde{\alpha}$ than to lower ones. A similar behavior for different atoms has been found in ref. [46].

In fig. C.2 the deviations $\varepsilon$ for different values of $1/\tilde{\alpha}$ are plotted as a color map for the first 600 states of basis set $(\tilde{\alpha}, 76, 30)$. One can see bands of states which are numerically converged (values smaller than $10^{-8}$) for a whole range of values of $\tilde{\alpha}$. Between those bands there are also bands of states which are more sensitive to a change of $\tilde{\alpha}$. This shows a non-uniform convergence of the spectrum not only up to higher states but also with convergence "gaps" corresponding to states which are worse approximated by the chosen basis set than states below and above them. Also it is visible that the optimal value for $\tilde{\alpha}$ is increasing for higher states. Thus for each state a corresponding optimal value for the convergence parameter has to be chosen. This has been done for the following comparison between different sizes of basis sets.

In fig. C.3 the deviations $\varepsilon$ are shown as a color map for different values of $1/\tilde{\alpha}$ and different states again for basis set $(\tilde{\alpha}, 76, 30)$. Additionally the deviation $\varepsilon$ for the same states is also shown for basis sets $(\tilde{\alpha}, N_{\max}, 30)$ with different $N_{\max}$. It is visible that the states in the bands which are numerically converged over a large interval of $\tilde{\alpha}$ values correspond to states which are also numerically converged already for smaller values of $N_{\max}$.

For the unscaled system of eq. (2.12) the quantum defects $\delta$ are plotted in fig. C.4 over the principal quantum number $n$ for basis sets $(\alpha, N_{\max}, 30)$ with different $N_{\max}$. Only the five states with larges $\delta$ have been plotted for better visibility. One can see that the physically correct behavior [4], a convergence to finite $\delta$, is only captured for sufficiently

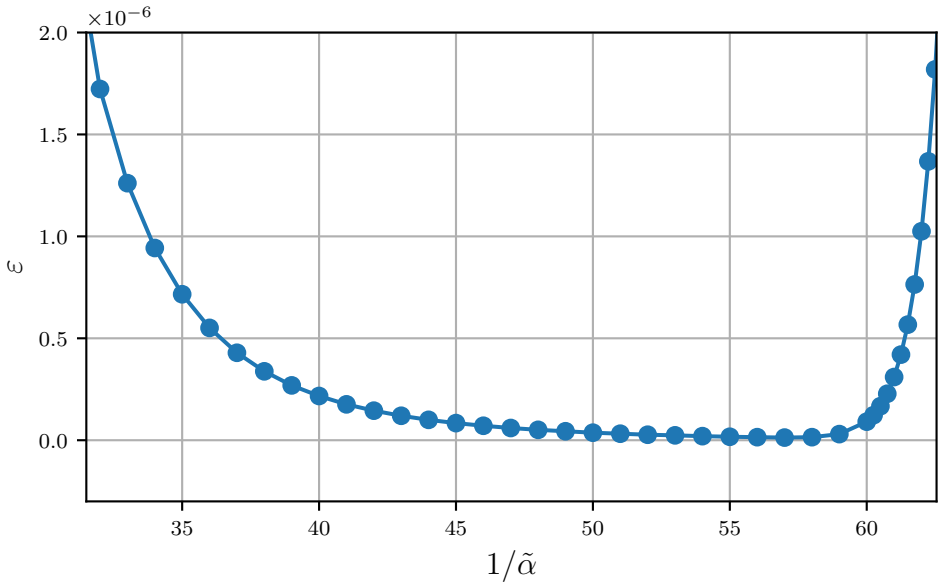


**Figure C.1:** Typical behavior of the deviations $\varepsilon$ to the optimal eigenvalue for different values of the convergence parameter $\tilde{\alpha}$ exemplary for one state.

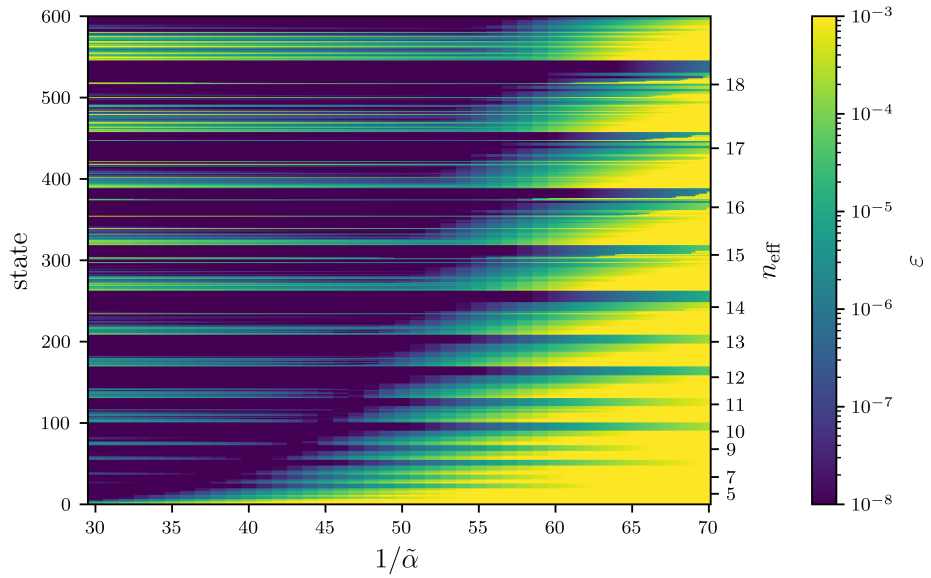


**Figure C.2:** Distance $\varepsilon$ to best $n_{\text{eff}}$ eigenvalue for different values of $\tilde{\alpha}$ and states exemplary for the basis set $(\tilde{\alpha}, 76, 30)$ of one block with odd parity. For the other block and states of even parity the results are similar.

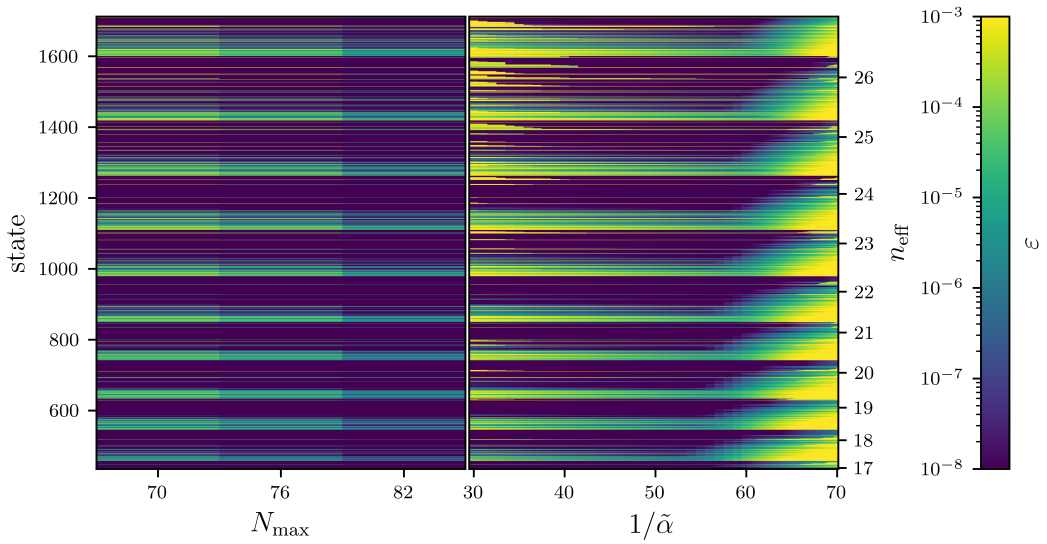


**Figure C.3:** Distance $\varepsilon$ to best $n_{\text{eff}}$ eigenvalue for different states and different $N_{\max}$ (left panel) or different values of $1/\tilde{\alpha}$ (right panel) exemplary for $N_{\max} = 76$. On can see that the eigenvalues are less sensitive to the choice of $\tilde{\alpha}$ values in a broader range when the convergence of the former is better already at lower $N_{\max}$ values. For all basis sets $L_{\max} = 30$ was used and the states are in one block of odd parity. For the other block and states of even parity the results are similar.

high values of $N_{\max}$. States with larger quantum defect have a stronger dependence on the basis size. Here they should be assignable to the states with smaller angular momentum quantum number $L$ according to their principal quantum number $n$ they first occur at. Note that this is only an approximate assignment as $L$ is not a good quantum number. For the unscaled system this gives a possibility to determine an appropriate basis size to achieve convergence up to a desired energy level with corresponding $n_{\text{eff}}$. The obtained value can then be used as a first estimation for the basis size needed for a scaled system to achieve convergence to the same $n_{\text{eff}}$ value. In fig. C.5 the typical convergence behavior for basis sets with increasing $N_{\max}$ is plotted. One can see that the gradient of the deviation to the best eigenvalue with respect to $N_{\max}$ is decreasing for increasing $N_{\max}$. In figs. C.6 and C.7 histograms over the change of the eigenvalues are shown for one block of odd parity if the basis set is change from $(\alpha, 82, 30)$ to $(\alpha, 84, 30)$. Only states with $n_{\text{eff}} < 30$ have been considered. It is visible that the majority of the states is already numerically converged as a large peak is visible in fig. C.6 for $\varepsilon < 1 \times 10^{-8}$. But there are still a few states with a comparable large change of $\varepsilon > 1 \times 10^{-4}$. The same overall behavior is also visible for the states of even parity as can be seen in figs. C.8 and C.9.

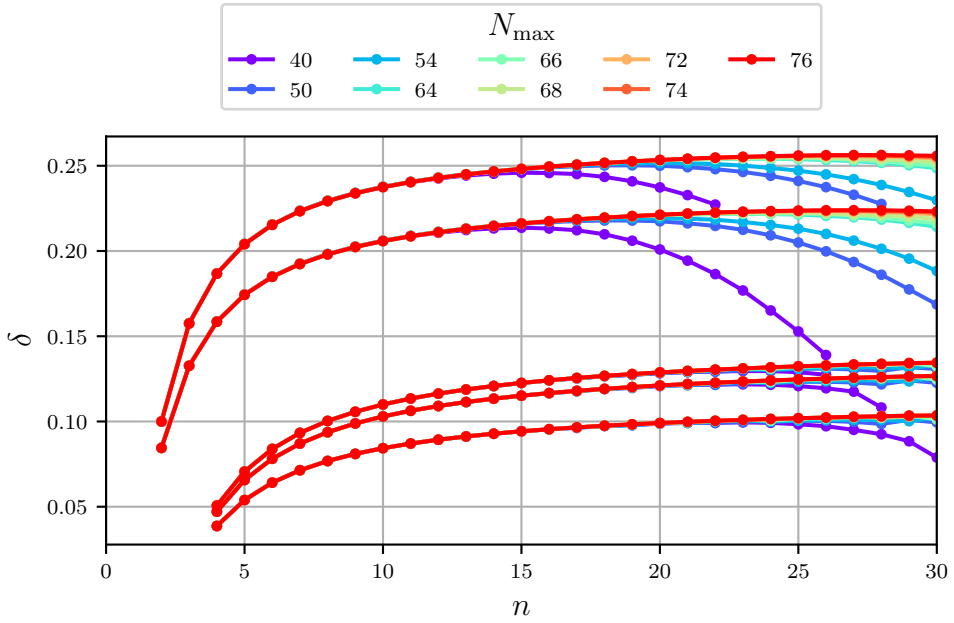


**Figure C.4:** Quantum defects $\delta$ for states in one block of odd parity for the unscaled system over principal quantum number $n$ for basis sets with different $N_{\max}$ and $L_{\max} = 30$.

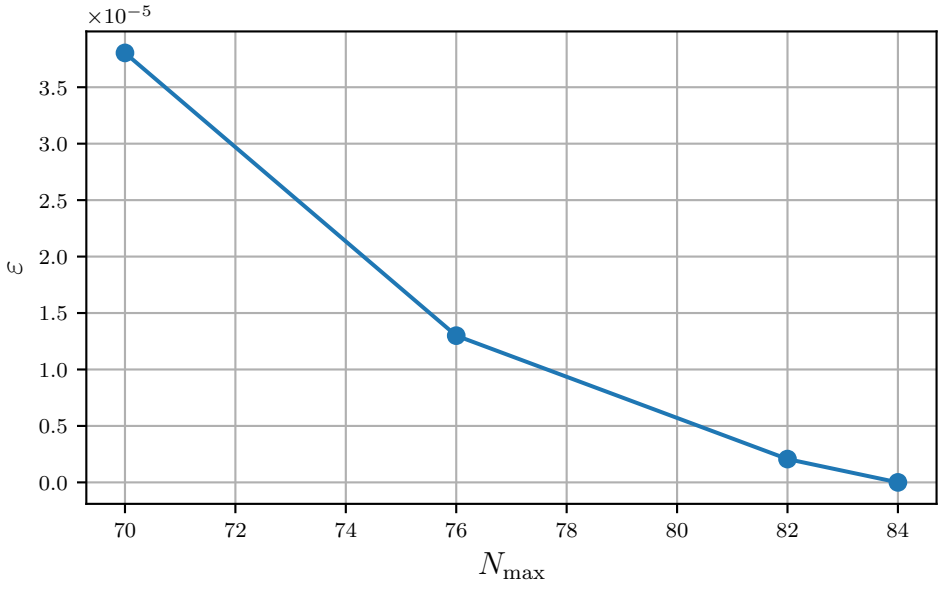


**Figure C.5:** Deviations $\varepsilon$ to best eigenvalue versus $N_{\max}$ with fixed $L_{\max} = 30$ exemplary for one state of odd parity.

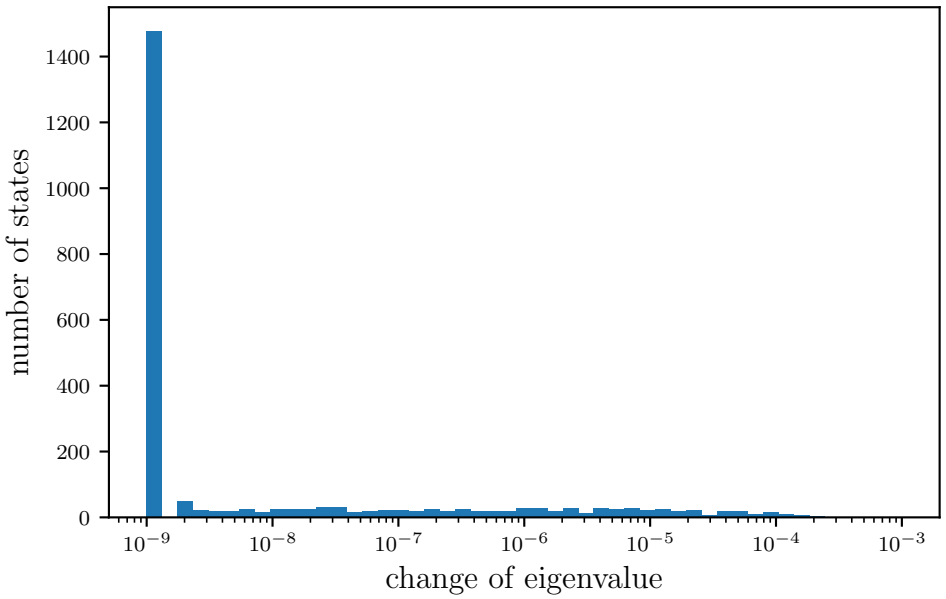


**Figure C.6:** Histogram over the change of the $n_{\text{eff}}$ eigenvalues between $(\tilde{\alpha}, 82, 30)$ and $(\tilde{\alpha}, 84, 30)$ for one block of odd parity.

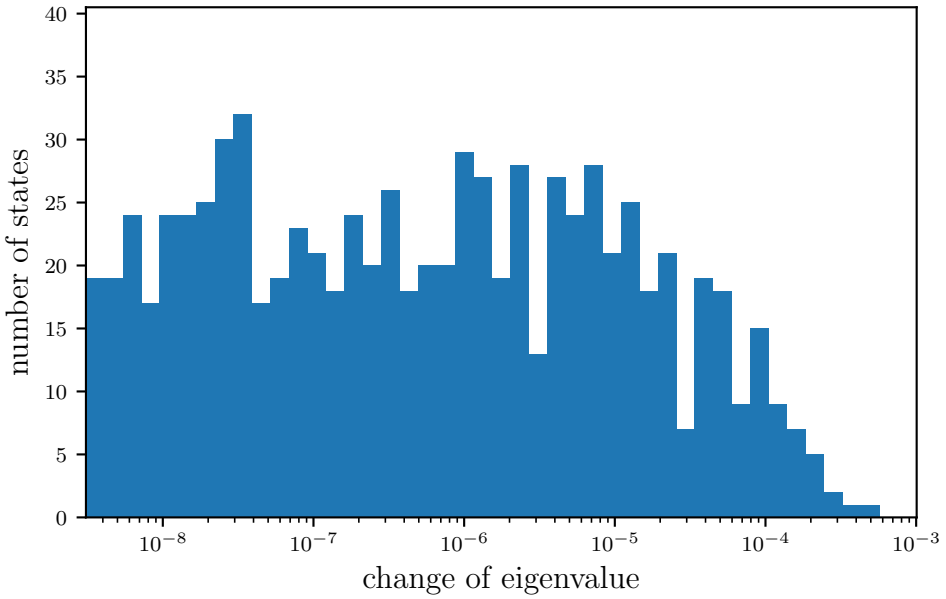


**Figure C.7:** Enlarged section of fig. C.6.

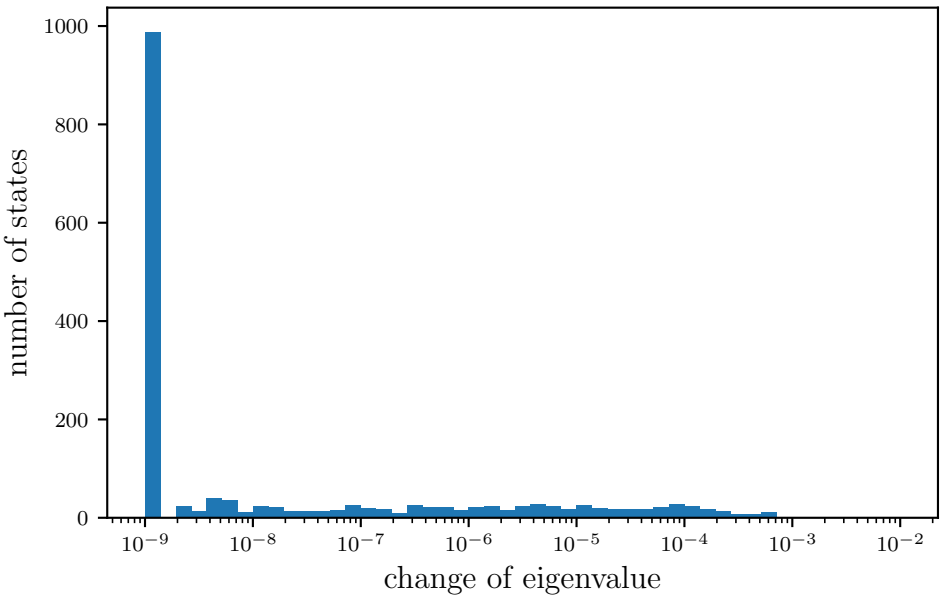


**Figure C.8:** Histogram over the change of the $n_{\text{eff}}$ eigenvalues between $(\tilde{\alpha}, 78, 30)$ and $(\tilde{\alpha}, 80, 30)$ for one block of even parity.

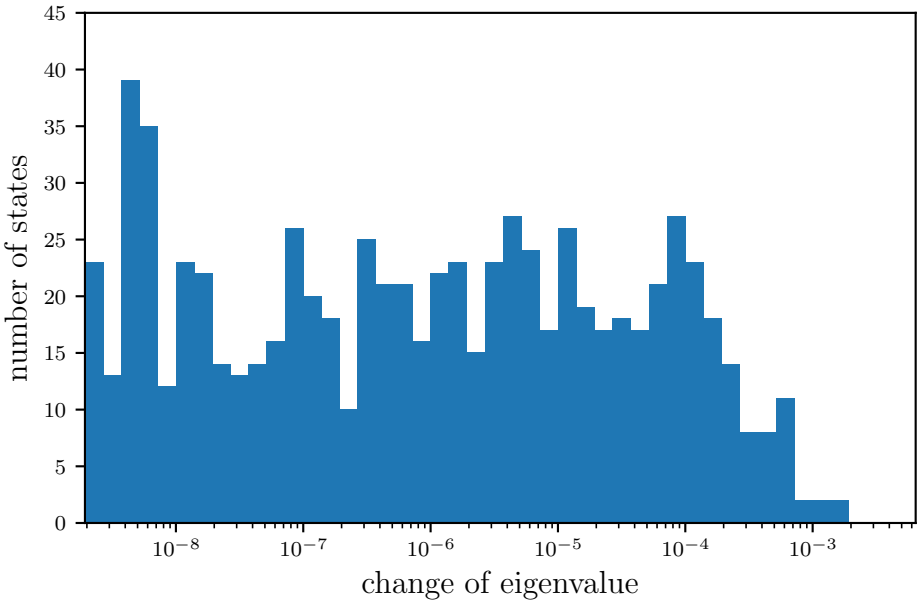


**Figure C.9:** Enlarged section of fig. C.8.

# Bibliography


[1] E. F. Gross. "Optical spectrum of excitons in the crystal lattice". In: *Il Nuovo Cimento (1955-1965)* 3 (1956), pp. 672–701. DOI: 10.1007/BF02746069.

[2] Tomasz Kazimierczuk, Dietmar Fröhlich, Stefan Scheel, Heinrich Stolz, and Manfred Bayer. "Giant Rydberg excitons in the copper oxide $Cu_2O$". In: *Nature* 514 (2014), pp. 343–347. DOI: 10.1038/nature13832.

[3] J. Thewes, J. Heckötter, T. Kazimierczuk, M. Aßmann, D. Fröhlich, M. Bayer, M. A. Semina, and M. M. Glazov. "Observation of High Angular Momentum Excitons in Cuprous Oxide". In: *Phys. Rev. Lett.* 115, 027402 (2015). DOI: 10.1103/PhysRevLett.115.027402.

[4] Florian Schöne, Sjard-Ole Krüger, Peter Grünwald, Marc Aßmann, Julian Heckötter, Johannes Thewes, Heinrich Stolz, Dietmar Fröhlich, Manfred Bayer, and Stefan Scheel. "Coupled valence band dispersions and the quantum defect of excitons in $Cu_2O$". In: *Journal of Physics B: Atomic, Molecular and Optical Physics* 49, 134003 (2016). DOI: 10.1088/0953-4075/49/13/134003.

[5] F. Schöne, S.-O. Krüger, P. Grünwald, H. Stolz, S. Scheel, M. Aßmann, J. Heckötter, J. Thewes, D. Fröhlich, and M. Bayer. "Deviations of the exciton level spectrum in $Cu_2O$ from the hydrogen series". In: *Phys. Rev. B* 93, 075203 (2016). DOI: 10.1103/PhysRevB.93.075203.

[6] Frank Schweiner, Jörg Main, Matthias Feldmaier, Günter Wunner, and Christoph Uihlein. "Impact of the valence band structure of $Cu_2O$ on excitonic spectra". In: *Phys. Rev. B* 93, 195203 (2016). DOI: 10.1103/PhysRevB.93.195203.

[7] Frank Schweiner, Jörg Main, Günter Wunner, and Christoph Uihlein. "Even exciton series in $Cu_2O$". In: *Phys. Rev. B* 95, 195201 (2017). DOI: 10.1103/PhysRevB.95.195201.

[8] Michael Victor Berry and Michael Tabor. "Closed orbits and the regular bound spectrum". In: *Proceedings of the Royal Society of London A* 349 (1976), pp. 101–123. DOI: 10.1098/rspa.1976.0062.

[9] Martin C. Gutzwiller. *Chaos in Classical and Quantum Mechanics*. Springer, New York, NY, 1990. DOI: 10.1007/978-1-4612-0983-6.

[10] Jörg Main. "Use of harmonic inversion techniques in semiclassical quantization and analysis of quantum spectra". In: *Physics Reports* 316 (1999), pp. 233–338. DOI: 10.1016/S0370-1573(98)00131-8.

[11] J. Main, P. A. Dando, Dz Belkic, and H. S. Taylor. "Decimation and harmonic inversion of periodic orbit signals". In: *Journal of Physics A: Mathematical and General* 33 (2000), pp. 1247–1263. DOI: 10.1088/0305-4470/33/6/311.

[12] Jan Ertl. "Adiabatic approximation for the dynamics of magnetoexcitons in $Cu_2O$". Master's thesis. Universität Stuttgart, 2019.

[13] Jan Ertl, Patric Rommel, Michel Mom, Jörg Main, and Manfred Bayer. "Classical and semiclassical description of Rydberg excitons in cuprous oxide". In: *Phys. Rev. B* 101, 241201 (2020). DOI: 10.1103/PhysRevB.101.241201.

[14] Michael Marquardt. "Semiclassical quantization for the states of cuprous oxide in consideration of the band structure". Master's thesis. Universität Stuttgart, 2021.

[15] J. Frenkel. "On the Transformation of light into Heat in Solids. I". In: *Phys. Rev.* 37 (1931), pp. 17–44. DOI: 10.1103/PhysRev.37.17.

[16] J. Frenkel. "On the Transformation of Light into Heat in Solids. II". In: *Phys. Rev.* 37 (1931), pp. 1276–1294. DOI: 10.1103/PhysRev.37.1276.

[17] Harald Ibach and Hans Lüth. *Festkörperphysik: Einführung in die Grundlagen*. Springer-Verlag, 2009. DOI: 10.1007/978-3-540-85795-2.

[18] Gregory H. Wannier. "The Structure of Electronic Excitation Levels in Insulating Crystals". In: *Phys. Rev.* 52 (1937), pp. 191–197. DOI: 10.1103/PhysRev.52.191.

[19] Mark Fox. *Optical Properties of Solids*. 3rd ed. Oxford University Press, 2010.

[20] Stephen A. Lynch, Chris Hodges, Soumen Mandal, Wolfgang Langbein, Ravi P. Singh, Liam A. P. Gallagher, Jon D. Pritchett, Danielle Pizzey, Joshua P. Rogers, Charles S. Adams, and Matthew P. A. Jones. "Rydberg excitons in synthetic cuprous oxide $Cu_2O$". In: *Phys. Rev. Materials* 5, 084602 (2021). DOI: 10.1103/PhysRevMaterials.5.084602.

[21] G. F. Koster, J. O. Dimmok, R. G. Wheeler, and H. Statz. *The Properties of the Thirty-Two Point Groups*. The MIT Press, 1963.

[22] A. Werner and H. D. Hochheimer. "High-pressure x-ray study of $Cu_2O$ and $Ag_2O$". In: *Phys. Rev. B* 25 (1982), pp. 5929–5934. DOI: 10.1103/PhysRevB.25.5929.

[23] Kristin Persson. *Materials Data on $Cu_2O$ (SG:224) by Materials Project*. 2014. DOI: 10.17188/1207131.

[24] Chihiro Hamaguchi. *Basic Semiconductor Physics*. 3rd ed. Springer, 2017. DOI: 10.1007/978-3-319-66860-4.

[25] Frank Schweiner. "Theory of excitons in cuprous oxide". PhD thesis. Universität Stuttgart, 2017.

[26] Ch. Uihlein, D. Fröhlich, and R. Kenklies. "Investigation of exciton fine structure in $Cu_2O$". In: *Phys. Rev. B* 23 (1981), pp. 2731–2740. DOI: 10.1103/PhysRevB.23.2731.

[27] G. Kuwabara, M. Tanaka, and H. Fukutani. "Optical absorption due to paraexciton of $Cu_2O$". In: *Solid State Communications* 21 (1977), pp. 599–601. DOI: 10.1016/0038-1098(77)90042-4.

[28] P. D. Bloch and C. Schwab. "Direct Evidence for Phonon-Assisted Transitions to the 1*s* Paraexciton Level of the Yellow Exciton Series in $Cu_2O$". In: *Phys. Rev. Lett.* 41 (1978), pp. 514–517. DOI: 10.1103/PhysRevLett.41.514.

[29] J. M. Luttinger. "Quantum Theory of Cyclotron Resonance in Semiconductors: General Theory". In: *Phys. Rev.* 102 (1956), pp. 1030–1041. DOI: 10.1103/PhysRev.102.1030.

[30] G. M. Kavoulakis, Yia-Chung Chang, and Gordon Baym. "Fine structure of excitons in $Cu_2O$". In: *Phys. Rev. B* 55 (1997), pp. 7593–7599. DOI: 10.1103/PhysRevB.55.7593.

[31] M French, R Schwartz, H Stolz, and R Redmer. "Electronic band structure of $Cu_2O$ by spin density functional theory". In: *Journal of Physics: Condensed Matter* 21, 015502 (2008). DOI: 10.1088/0953-8984/21/1/015502.

[32] Claus F. Klingshirn. *Semiconductor optics*. 4th ed. Springer, Berlin, Heidelberg, 2012. DOI: 10.1007/978-3-642-28362-8.

[33] A. Baldereschi and Nunzio O. Lipari. "Spherical Model of Shallow Acceptor States in Semiconductors". In: *Phys. Rev. B* 8 (1973), pp. 2697–2709. DOI: 10.1103/PhysRevB.8.2697.

[34] J. R. Rydberg. "XXXIV. On the structure of the line-spectra of the chemical elements". In: *The London, Edinburgh, and Dublin Philosophical Magazine and Journal of Science* 29 (1890), pp. 331–337. DOI: 10.1080/14786449008619945.

[35] James E. Bayfield. *Quantum Evolution. An Introduction to Time-Dependent Quantum Mechanics*. John Wiley & Sons, Inc., 1999.

[36] Sandro Wimberger. *Nonlinear Dynamics and Quantum Chaos. An Introduction*. 1st ed. Springer, Cham, 2014. DOI: 10.1007/978-3-319-06343-0.

[37] Michael V. Berry and Michael Tabor. "Calculating the bound spectrum by path summation in action-angle variables". In: *Journal of Physics A: Mathematical and General* 10 (1977), pp. 371–379. DOI: 10.1088/0305-4470/10/3/009.

[38] Denis Ullmo, Maurice Grinberg, and Steven Tomsovic. "Near-integrable systems: Resonances and semiclassical trace formulas". In: *Phys. Rev. E* 54 (1996), pp. 136–152. DOI: 10.1103/PhysRevE.54.136.

[39] Ch. Uihlein, D. Fröhlich, and R. Kenklies. "Investigation of exciton fine structure in $Cu_2O$". In: *Phys. Rev. B* 23 (1981), pp. 2731–2740. DOI: 10.1103/PhysRevB.23.2731.

[40] M. A. Caprio, P. Maris, and J. P. Vary. "Coulomb-Sturmian basis for the nuclear many-body problem". In: *Phys. Rev. C* 86, 034312 (2012). DOI: 10.1103/PhysRevC.86.034312.

[41] E. Joachim Weniger. "Weakly convergent expansions of a plane wave and their use in Fourier integrals". In: *Journal of Mathematical Physics* 26 (1985), pp. 276–291. DOI: 10.1063/1.526970.

[42] Bruno Klahn and Werner A. Bingel. "The convergence of the Rayleigh-Ritz method in quantum chemistry I." In: *Theoretica Chimica Acta* 44 (1977), pp. 9–26. DOI: 10.1007/BF00548026.

[43] Bruno Klahn and Werner A. Bingel. "The convergence of the Rayleigh-Ritz method in quantum chemistry II." In: *Theoretica Chimica Acta* 44 (1977), pp. 27–43. DOI: 10.1007/BF00548027.

[44] E. Anderson, Z. Bai, C. Bischof, S. Blackford, J. Demmel, J. Dongarra, J. Du Croz, A. Greenbaum, S. Hammarling, A. McKenney, and D. Sorensen. *LAPACK Users' Guide*. Third. Philadelphia, PA: Society for Industrial and Applied Mathematics, 1999.

[45] Rudolph Peierls. *Surprises in Theoretical Physics*. Princeton University Press, 1979.

[46] Michael Friedrich Herbst. "Development of a modular quantum-chemistry framework for the investigation of novel basis functions". PhD thesis. Ruprecht-Karls-Universität Heidelberg, 2018.

[47] Olgierd Cecil Zienkiewicz, Robert Leroy Taylor, and Jian Z. Zhu. *The Finite Element Method: Its Basis and Fundamentals*. 7th ed. Elsevier, 2013. DOI: 10.1016/C2009-0-24909-9.

[48] William H. Press, Saul A. Teukolsky, Brian P. Flannery, and William T. Vetterling. *Numerical Recipes in FORTRAN 77. The Art of Scientific Computing*. 2nd ed. Vol. 1. Cambridge University Press, 1992.

[49] Matthias Brack and Rajat K. Bhaduri. *Semiclassical physics*. Addison-Wesley Publishing Company, Inc., 1997.

[50] Jan Ertl. private communication. 2021.

[51] Jan Ertl, Michael Marquardt, Moritz Schumacher, Patric Rommel, Jörg Main, and Manfred Bayer. "Direct observation of exciton orbits in quantum mechanical recurrence spectra of $Cu_2O$". In: *Phys. Rev. Lett.* (2021). Submitted.

[52] J. W. Hodby, T. E. Jenkins, C. Schwab, H. Tamura, and D. Trivich. "Cyclotron resonance of electrons and of holes in cuprous oxide, $Cu_2O$". In: *Journal of Physics C: Solid State Physics* 9 (1976), pp. 1429–1439. DOI: 10.1088/0022-3719/9/8/014.

[53] O. Madelung, U. Rösler, and M. (editors) Schulz. *Landolt-Börnstein - Group III Condensed Matter*. Berlin Heidelberg: Springer-Verlag, 1998.

# Zusammenfassung in deutscher Sprache

Die Energiedispersion in einem Festkörper ist gegeben durch dessen Bandstruktur. Wird ein Elektron aus einem Valenzband in das Leitungsband angeregt, entsteht ein unbesetzter Zustand im ersteren. Dieser kann durch ein positiv geladenes Quasiteilchen beschrieben werden, welches Loch genannt wird. Durch die Coulombanziehung zwischen Loch und Elektron existieren gebundene Zustände welche als Exzitonen bezeichnet werden. Dies legt eine Beschreibung in Analogie zum Wasserstoffatom nahe. Tatsächlich ist diese Näherung gültig wenn bestimmte Voraussetzungen erfüllt sind. So müssen die Exzitonen zum Beispiel eine genügend große Ausdehnung im Ortsraum aufweisen, damit der Kristallhintergrund als Kontinuum beschrieben werden kann.

Für die in dieser Arbeit untersuchten Exzitonen in Kupferoxydul ($Cu_2O$) ist eine solche wasserstoffähnliche Beschreibung eine gute erste Näherung. Je nachdem welche Valenz- und Leitungsbänder bei der Anregung beteiligt sind unterscheidet man zwischen verschiedenen Exzitonserien. Diese werden nach der Farbe des Lichts benannt welches für deren Anregung benötigt wird. Die beiden Serien mit den niedrigsten Anregungsenergien heißen dementsprechend gelbe und die grüne Serie. Die gelbe Serie mit der niedrigsten Anregungsenergie war Gegenstand intensiver experimenteller Untersuchungen [1–3] und ein wasserstoffähnliches Exzitonspektrum konnte beobachtet werden. Es wurden jedoch auch Abweichungen vom wasserstoffähnlichen Verhalten festgestellt welche als Feinstrukturaufspaltung im Spektrum sichtbar sind [3]. Theoretische Untersuchungen konnten diese hauptsächlich der komplexen Bandstruktur zuordnen [4–6]. Für eine genauere theoretische Beschreibung der gelben Exzitonen muss eine vorhandene Kopplung zur grünen Serie berücksichtigt werden [7], was eine Miteinbeziehung der an dieser Serie beteiligten Valenzbänder erfordert. Dies kann durch die Einführung eines Quasispins erreicht werden, der mit dem Lochspin koppelt. Die Stärke der Kopplung der beiden Serien wird durch die Spin-Orbit Kopplungskonstante $\Delta$ bestimmt, deren Wert durch den Abstand zwischen den an den beiden Serien beteiligten Valenzbändern am $\Gamma$-Punkt gegeben ist.

Im Jahre 2014 konnten hoch angeregte gelbe Exzitonzustände mit einer Hauptquantenzahl von bis zu $n = 25$ von T. Kazimierczuk et al. [2] experimentell nachgewiesen werden.

Für diese großen Quantenzahlen kann das Korrespondenzprinzip angewandt werden und eine klassische beziehungsweise semiklassische Beschreibung wird möglich. In dieser Arbeit wollen wir Verbindungen zwischen dem quantenmechanischen Spektrum und der zugeordneten klassischen Dynamik für die Exzitonen der gelben Serie untersuchen. Wir berücksichtigen dabei die komplexe Valenzbandstruktur die an der gelben und grünen Serie beteiligt ist und damit die Abweichungen vom wasserstoffähnlichen Fall. Numerische quantenmechanische Rechnungen erfordern die Diagonalisierung eines Hamiltonian in einer großen, abgeschnittenen Basis. Obwohl die Ergebnisse sehr gut mit Experimenten übereinstimmen [7] bieten diese keine direkten Informationen über die zugeordnete klassische Dynamik. Für wasserstoffähnliche Systeme sind klassische Keplerellipsen mit dem Rydbergspektrum über das Bohr-Sommerfeld-Modell verknüpft. Die klassische Phasenraumstruktur ändert sich nicht mit der Energie, da sich alle gebundenen Zustände mit klassischen elliptischen Keplerbahnen verknüpfen lassen. Für Exzitonen in $Cu_2O$ ist dies nicht der Fall. Die zugeordnete klassische Dynamik ändert sich für jeden Zustand im Spektrum, da sich das Verhältnis zwischen der entsprechenden Energie und der Spin-Orbit Kopplungskonstante $\Delta$ ändert. Es ist möglich diese Energieabhängigkeit zu umgehen, indem die Kopplungskonstante $\Delta$ so mit der Energie skaliert wird, dass das Verhältnis zwischen Energie und resultierender skalierter Kopplungskonstante $\tilde{\Delta}$ über das gesamte Spektrum konstant bleibt. Dies führt zu einem skalierten Quantenspektrum. Für jede gebundene klassische Dynamik, gekennzeichnet durch eine gegebene Energie, existiert ein entsprechendes skaliertes Quantenspektrum.

Eine Verbindung zwischen den quantenmechanischen Exzitonspektren und der klassischen Exzitondynamik wird durch semiklassische Spurformeln hergestellt [8, 9]. Diese verknüpfen Fluktuationen in der quantenmechanischen Zustandsdichte mit einer Überlagerung von Oszillationen mit Frequenzen bestimmt durch die Periode oder Wirkung von klassischen periodischen Orbits. Deren Amplituden sind verknüpft mit den Stabilitätseigenschaften der Orbits. Wir wenden daher eine Fouriertransformation und eine Technik für hochauflösende Spektralanalyse, genannt harmonische Inversion, auf die numerisch berechneten skalierten quantenmechanischen Exzitonspektren an. Die sich ergebenden Wiederkehrspektren zeigen Maxima an Positionen gegeben durch die Wirkung von klassischen periodischen Bahnen der zugeordneten klassischen Dynamik. Deren Anteil am Quantenspektrum ist gegeben durch die Amplitude der Maxima.

Durch geeignete Miteinbeziehung der Bandstruktur von $Cu_2O$ ist eine klassische Behandlung der Exzitonen möglich [12–14]. Durch die Anwendung von semiklassischen Theorien kann ein semiklassisches Wiederkehrspektrum mit den Parametern von numerisch integrierten klassischen periodischen Bahnen erstellt werden [14]. Ein Vergleich zwischen quantenmechanischen und semiklassischen Wiederkehrspektren zeigt eine gute Übereinstimmung. Dies erlaubt es Informationen über die periodischen Bahnen zu erhalten (zum Beispiel Form, Wirkung, Stabilität, etc.) die zum skalierten Quantenspektrum beitragen.

Diese Arbeit liefert damit einen tieferen Einblick in die klassische Exzitondynamik in $Cu_2O$ und die Beziehung zwischen der Feinstrukturaufspaltung im Quantenspektrum und der zugeordneten klassischen Dynamik.

# Danksagung

An dieser Stelle möchte ich mich bei all denjenigen bedanken, die mich bei der Erstellung dieser Arbeit unterstützt haben. Einen besonderen Dank möchte ich an folgende Personen richten:

- Herr Prof. Dr. Jörg Main für die Möglichkeit dieses spannende Thema zu bearbeiten, die hervorragende Betreuung und die hilfreichen Diskussionen.
- Herr Prof. Dr. Udo Seifert für die Übernahme des Mitberichtes.
- Herr M. Sc. Patric Rommel für die Unterstützung bei der Berechnung der Exzitonspektren und hilfreichen Diskussionen.
- Herr M. Sc. Jan Ertl und Herr M. Sc. Michael Marquardt für die gute Zusammenarbeit auf dem Gebiet der Exzitonen in Kupferoxydul und die Bereitstellung der klassischen und semiklassischen Ergebnisse. Ohne diese wären die Erkenntnisse dieser Arbeit nicht möglich gewesen. Herr M. Sc. Jan Ertl danke ich des weiteren für die hilfreiche Unterstützung bei offenen Fragen.
- Herr M. Sc. Johannes Reiff für die hervorragende Systemadministration.
- Frau Monika Bund für die Unterstützung bei verwaltungstechnischen Aufgaben.
- Alle weiteren Mitarbeiter des Instituts für Theoretische Physik I für die tolle Atmosphäre und die interessanten Gespräche in der (virtuellen) Kaffeerunde, die die Zeit an diesem Institut zu einer tollen Erfahrung gemacht haben, trotz Coronapandemie.
- Meine Eltern für die vielseitige Unterstützung während des gesamten Physikstudiums und dieser Masterarbeit.

**Erklärung**

Ich versichere,

- dass ich diese Masterarbeit selbstständig verfasst habe,
- dass ich keine anderen als die angegebenen Quellen benutzt und alle wörtlich oder sinngemäß aus anderen Werken übernommenen Aussagen als solche gekennzeichnet habe,
- dass die eingereichte Arbeit weder vollständig noch in wesentlichen Teilen Gegenstand eines anderen Prüfungsverfahrens gewesen ist,
- und dass das elektronische Exemplar mit den anderen Exemplaren übereinstimmt.

Stuttgart, den 24. November 2021 *Moritz Schumacher*